Interface engineering of MXene-based heterostructures for lithium-sulfur batteries

Siyu Wu[1], Xiang Li[1], Yongzheng Zhang[1,2] (✉), Qinghua Guan[3], Jian Wang[3,4] (✉), Chunyin Shen[1], Hongzhen Lin[3], Jitong Wang[1], Yanli Wang[1], Liang Zhan[1] (✉), and Licheng Ling[1]

[1] *State Key Laboratory of Chemical Engineering, East China University of Science and Technology, 130 Meilong Road, Shanghai 200237, China*

[2] *Key Laboratory of Specially Functional Polymeric Materials and Related Technology (Ministry of Education), School of Chemical Engineering, East China University of Science and Technology, 130 Meilong Road, Shanghai 200237, China*

[3] *i-Lab & CAS Key Laboratory of Nanophotonic Materials and Devices, Suzhou Institute of Nano-tech and Nano-bionics, Chinese Academy of Sciences, Suzhou 215123, China*

[4] *Helmholtz Institute Ulm (HIU), Ulm D89081, Germany*

ABSTRACT

High energy density and low cost make lithium-sulfur (Li-S) batteries as one of the next generation's promising energy storage systems. However, the following problems need to be solved before commercialization: (i) the shuttling effect and sluggish redox kinetics of lithium polysulfides in sulfur cathode; (ii) the formation of lithium dendrites and the crack of solid electrolyte interphase; (iii) the large volume changes during charge and discharge processes. MXenes, as newly emerging two-dimensional transition metal carbides/nitrides/carbonitrides, have attracted widespread attention due to their abundant active surface terminals, adjustable vacancies, and high electrical conductivity. Designing MXene-based heterogeneous structures is expected to solve the stacking problem induced by hydrogen bonds or Van der Waals force and to provide other charming physiochemical properties. Herein, we generalize the design principles of MXene-based heterostructures and their functions, i.e., adsorption and catalysis in advanced conversion-based Li-S batteries. Firstly, the physiochemical properties of MXene and MXene-based heterostructures are briefly introduced. Secondly, the catalytic functions of MXene-based heterostructures with the compositional constituents including carbon materials, metal compounds, organic frameworks, polymers, single atoms and special high-entropy MXenes are comprehensively summarized in sulfur cathodes and lithium anodes. Finally, the challenges of MXene-based heterostructure in current Li-S batteries are pointed out and we also provide some enlightenments for future developments in high-energy-density Li-S batteries.

KEYWORDS

MXene, heterostructures, lithium-sulfur battery, shuttle effect, interface engineering

1 Introduction

As the depletion of global energy resources and the ever-growing demands for portable electronic devices, electric vehicles and smart power grids, the targets of carbon neutrality and carbon peak are put forward [1–6]. Against such backgrounds, the value chain of clean energy and low-carbon technology such as lithium-ion batteries (LIBs) have become the top priority. However, the state-of-art energy densities of commercial LIBs have almost reached their ceiling, which will be difficult to meet the future market demand of higher energy density to drive a long distance or extend operation time [7, 8]. Therefore, exploring and developing a substitutable energy storage system with high specific and volumetric energy density is of great importance [9, 10].

Among various anodic materials, lithium anode is known as the "holy grail" and "ultimate anode" due to its remarkable theoretical specific capacity (3680 mAh·g^{-1}) and the lowest electrochemical potential (−3.04 V versus standard hydrogen electrode) [11–18]. By matching conversion-based sulfur cathode, the lithium-sulfur (Li-S) batteries output a theoretical specific capacity of 1675 mAh·g^{-1} (Fig. 1(a)). Together with an average operating voltage of 2.15 V, Li-S batteries can achieve a superior theoretical energy density of up to 2600 Wh·kg^{-1}, which is considered to be one of the most attractive next-generation energy storage devices [19–22]. Furthermore, different from the intercalation-typed lithiated transition metal oxides, the elemental sulfur is rich in natural content and environmentally friendly, which showcases great prospects for low-cost large-scale application in the future [23, 24]. The operation of Li-S batteries relies on the reversible redox reaction between Li and S_8 (Fig. 1(b)).

$$S_8 + 16Li \leftrightarrow 8Li_2S$$

Actually, in the charging/discharging processes, the Li-S batteries experience quite complicated processes with multi-step redox reactions and triphasic changes. Firstly, the intermediate lithium polysulfides (LiPSs) are easily dissolved in the electrolyte and tend to migrate to the lithium anode, forming polysulfide shuttling and deteriorating the metallic lithium anode. The severe shuttle effect

Address correspondence to Yongzheng Zhang, zhangyongzheng@ecust.edu.cn; Jian Wang, jian.wang@kit.edu; Liang Zhan, zhanliang@ecust.edu.cn

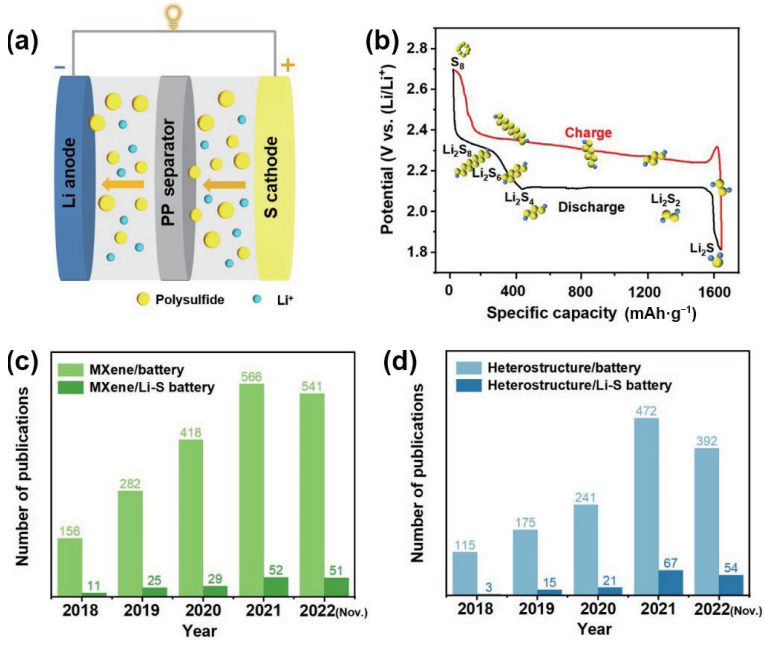

Figure 1 (a) Schematic diagram and (b) a representative charge–discharge voltage curve of Li-S batteries. (c) and (d) The number of recent five years publications on MXene and heterostructures in Li-S batteries. Data adopted from Web of Science on Nov, 4th, 2022.

leads to slow redox kinetics, resulting in loss of active materials in cathode and terrible capacity attenuation [25, 26]. Secondly, the sluggish Li stripping/plating kinetics and uneven distribution in the anodic side lead to the formation of fatal lithium dendrites and the crack of formed solid electrolyte interphase (SEI) during repeated charge and discharge processes, exhausting the limited amount of electrolyte [27]. To make matters worse, continuous growth of lithium dendrites can puncture the separator and cause short circuit of batteries. Moreover, the large volumetric changes induce the active materials detachment from the electrode, aggravating the capacity loss.

Countless researches about rationally designed hosts or protective materials come one after another in the past decades, and these strategies include (i) physically confining sulfur, chemically bonding with LiPSs by heteroatoms and polar metal or metal compounds; (ii) introducing multi-functional catalysts to enhance the kinetics of sulfur redox conversions; (iii) designing advanced Li anode hosts or artificial SEI layers to homogeneously guide the Li nucleation and growth, thus suppressing the dendrite formation [28–38]. In comparison with traditional materials such as carbons, polymers, and other metal-based compounds (Table 1), MXenes (transition metal carbides, carbonitrides or nitrides) are promising candidates due to the key features of high electrical conductivity, adjustable terminals, rich defects and vacancies, large specific surface area and good mechanical strength, offering unlimited possibilities for applications in both sulfur cathodes and lithium anodes. However, the hydrogen bonds and Van der Waals forces within layers make MXene nanosheets stack easily, limiting rapid transportation of ions and effective exposure of active sites. Rationally constructing MXene-based heterogeneous structures endows the composites with favorable physicochemical properties to satisfy multiple requirements, which can solve these problems hopefully. Moreover, the rapidly increasing number of literature reports on MXene or their heterostructures in Li-S batteries demonstrates the potential of using in the electrochemical fields (Figs. 1(c) and 1(d)). However, up to date, there is no comprehensive review about the designing principles of MXene-based heterostructures in conversion-based Li-S batteries.

Herein, a comprehensive overview of recent advances in MXene-based heterostructures for Li-S batteries is summarized from structural design to catalytic sulfur redox reaction to indue lithium metal deposition. Firstly, the properties of MXene and MXene-based heterostructures are illustrated. Then, we classify MXene-based heterostructures into six main types from the aspects of compositional constituents and elaborate on their recent progresses applied in sulfur cathode and Li anode for high performance Li-S batteries (Fig. 2). Finally, we expound a concise outlook on the future research directions of MXene-based heterostructures and provide some inspirations for the design and fabrication of advanced Li-S batteries.

2 Properties of MXene and MXene-based heterostructures

2.1 Properties of MXene

MXenes ($M_{n+1}X_nT_x$) is a novel family of two-dimensional (2D) materials obtained by etching of A-layer atoms from their MAX phase, in which "M" represents the early transition metal (such as Ti, V, Zr and Nb); "A" represents the third or fourth main group elements (such as Al, Ga, and Si); "X" represents carbon or nitrogen; "T_x" represents the terminations left on the surface of MXene after etching, such as –O, –OH, –F, –S, –Cl, and $–NH_2$, respectively [39–43]. MXenes are usually prepared by selective etching lamination of "A" layer in MAX phases, including but not limited to HF etching, alkali etching, molten salt etching, and electrochemical etching [44–48]. Since Yury and co-workers discovered the $Ti_3C_2T_x$-MXene for the first time in 2011, due to its large specific surface area (ranging from 250 to 1000 $m^2 \cdot g^{-1}$) high conductivity (up to 1.51×10^6 $S \cdot cm^{-1}$) and rich functional terminals (Fig. 3), MXene has a wide application prospect in the energy storage fields including lithium-ion battery, sodium-ion battery, Li-S battery, supercapacitor and so on [49–57].

Taking Li-S battery for example, the metallic conductivity of MXene provides rapid electron transfer to maximize sulfur utilization. Moreover, MXenes, as 2D materials, have large specific surface area characteristics, providing a sufficient surface for electrochemical reactions and efficiently constructing three-dimensional (3D) composite materials for sulfur cathodes or lithium anode hosts [58]. MXenes are highly hydrophilic; their

Table 1 The advantages and disadvantages of MXene compared with other traditional materials

Materials	Advantages	Disadvantages
MXene	● High electronic conductivity ● Large surface area ● Abundant terminal functional group	● Layer stacking
Carbon	▸ High electronic conductivity ▸ Feasible synthesis & modification	▸ Low volumetric density
Metal compounds	▪ Polar active sites ▪ High electronic conductivity	▪ High weight ▪ Low porosity
Organic polymer	♦ Robust flexibility ♦ Rich heteroatom	♦ Poor electrochemical stability ♦ Poor conductivity

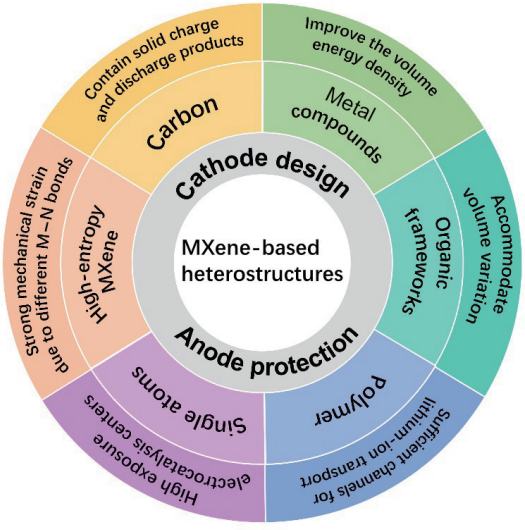

Figure 2 An overview of MXene-based heterostructures categories for cathode design and anode protection

abundant surface terminations make them easily dispersed in water and most polar organic solvents. Furthermore, sufficient surface terminations can induce uniform nucleation and suppress the growth of lithium dendrites [59, 60]. At the same time, the metal centers and polar functional groups on the surface of MXenes can bond with LiPSs. Theoretical studies have proved that most MXenes are suitable adhesives for LiPSs chemisorption [61, 62]. Nazar's team found that the hydroxyl groups on $Ti_3C_2T_x$-MXene were converted to thiosulfate after contacting with polysulfides, and then Ti–S bonds were formed between Ti atoms exposed on MXene and polysulfides through Lewis acid–base interaction [63]. The adsorbed polysulfides were transformed into Li_2S by electron transfer of MXene and formed multiple nucleation sites for Li_2S. Besides, the catalytic ability of MXenes is significantly affected by the terminations and vacancies on MXene. Wei's group reported that the adsorption energy of Li_2S_8 on $Ti_3C_2Cl_2$ possessing 1/16 Cl deficiencies increased from 0.7–1.1 to 2.5–3.5 eV, meaning improved anchoring and catalytic ability of $Ti_3C_2T_x$ to boost the electrochemical performance of Li-S batteries [64]. MXenes also exhibit good mechanical stability due to M–C or M–N bond with high bonding strength, so they can adapt to the large volume change of sulfur cathode in the charge–discharge processes. It can be seen that MXenes combine all these benefits together compared to other 2D materials (graphene, layered hydroxides, etc.). Therefore, it is considered that MXenes have strong potential for building high performance Li-S batteries.

2.2 Properties of MXene-based heterostructures

Although MXene endows Li-S batteries with a high specific capacity, efficient ion transportation, and durable electrochemical stability, the tendency of layered MXenes to stack again limits the electron/ion transportation along the vertical direction between layers, sacrificing the electrochemical performance of Li-S batteries at high sulfur loading and content [65]. Moreover, it is difficult for a certain kind of MXene to balance the physical capture, chemisorption, and catalytic conversion of LiPSs, which can only improve the performance of Li-S batteries to a limited extent. Therefore, it is considered that the construction of heterogeneous structures based on MXenes can achieve synergistic effects and endue the composite with specified physical and chemical properties to meet various requirements [66, 67].

W. Shockley first proposed the concept of heterostructure in semiconductor physics [68]. According to the definition, heterostructure consists of different semiconductors with similar crystal structures, similar atomic spacings, and thermal expansion coefficients. An interface is formed within the heterogeneous structure, in which chemical composition, charge distribution, and even some physicochemical properties change due to the band structure, carrier concentration, and Fermi level differences [69, 70]. Firstly, the MXene-based heterostructure electrodes can combine the advantages of different components to make up for the shortcomings of MXene, thus providing more active sites and promoting charge transfer (Fig. 4). Secondly, the internal electric field will be introduced at the interface of the heterogeneous structure to accelerate the ion diffusion kinetics. Last but not the least, the construction of heterostructure can adjust the electronic structure and coordination environment, inducing more active sites for adsorption and catalysis. Consequently, the synergistic effect of the heterogeneous structure significantly improves the corresponding electrocatalytic performance and reversible capacity of Li-S batteries.

3 MXene-based heterostructures reinforced sulfur redox kinetics

Owing to the insulative nature of S/Li_2S, polysulfide shuttling, and sluggish redox kinetics, an ideal sulfur cathode should satisfy the following characteristics: (i) excellent electroconductivity to provide unobstructed ion transport channels; (ii) abundant anchoring sites to strengthen the physical/chemical adsorption ability to LiPSs; (iii) rich catalytic sites to propel the redox conversions of LiPSs; (iv) large specific surface area to afford high sulfur loading and Li_2S deposition. Considering the above requirements, the reasonable designs of MXene-based heterostructures in Li-S batteries have received intensive attention. As expected, the heterostructure design directly incorporates the distinctions of various components. The combination of other materials with MXene can alleviate the restacking of MXene nanosheet, enhance the affinity to LiPSs and accelerate the sulfur redox reactions. In this section, multi-functional MXene-based heterostructures for sulfur cathodes are categorized as MXene-carbon, MXene-metal compounds, MXene-polymer, MXene-organic framework, MXene-single atom and high-entropy MXene catalyst heterostructures. A concise overview is summarized in Table 2 (separator modification coating belongs to the cathode in this review).

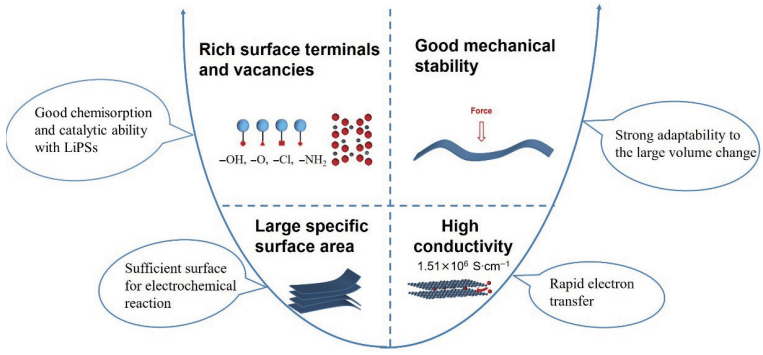

Figure 3 Unique properties of MXene toward Li-S batteries

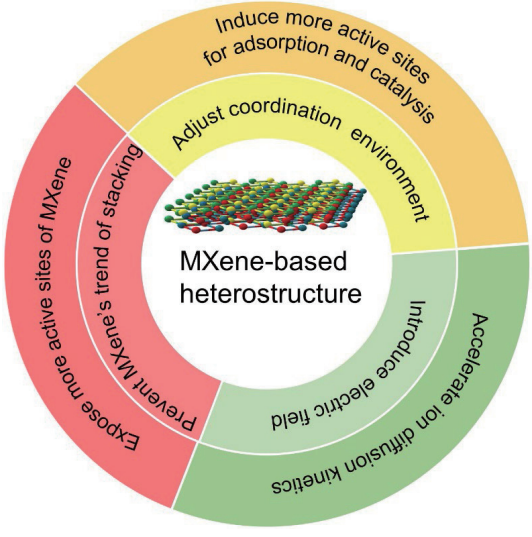

Figure 4 Properties of MXene-based heterostructures on Li-S batteries

3.1 MXene-carbon heterostructures

As pointed out by previous studies, 2D MXenes (Ti_2C as an example) have been proven to be chemisorbed by polysulfides at the Ti site, forming the weak metal–sulfur bond [63]. However, due to the instability and self-interaction behaviors via strong hydrogen bonds and Van der Waals forces, MXenes show a tendency of irreversible restacking, resulting in the decrease of surface area and the loss of exposed active sites, limiting its functions in adsorbing LiPSs [103, 104]. Carbonaceous materials exhibit the advantages in light weight, excellent electroconductivity, large specific surface area and electrochemical stability to accommodate sulfur species [105]. For example, graphene oxide (GO), carbon nanotubes (CNTs), and porous carbon materials have been confirmed to physically confine the LiPSs with acceptable electronic conductivity [106–113]. The introduction of carbon into MXene can not only act as a spacer insertor to prevent the stacking of MXene nanosheets but also achieve rapid cross-linked electronic transport.

Nazar and her colleagues incorporated CNTs into the MXene phase as sulfur host to prevent the restacking of delaminated MXene nanosheets [63]. A conductive network is formed by interweaving CNTs into the MXene layers. The hydroxyl groups on the surface of MXene can oxidize polysulfides to form thiosulfate groups, followed by the Wackenroder reaction and exposure of Ti atoms. Besides, strong Lewis acid–base interactions induce the formation of Ti–S bonds between the exposed Ti atoms and polysulfide-ion orbitals (Fig. 5(a)) [114]. The polysulfides instead of hydroxyl gradually act as the terminal group on the MXene nanosheet, and the fully exposed MXene exhibits the highest binding energy with LiPSs. The effects of dual polysulfide entrapment mechanism and conductive network design afford the sulfur cathode with superb long-term cycling. To further improve the porosity and conductivity of MXene-CNT heterostructure at high sulfur loading, the sandwich-like structured MXene/CNT/MXene aerogel was prepared by the unidirectional low-temperature freeze-drying method (Fig. 5(b)) [71]. When the mixed dispersion of CNTs and MXene was immersed into liquid nitrogen, MXene precipitated along the ice crystal surface and sandwiched the CNTs in the middle due to the CNTs wrapped by PVP precipitating more slowly than MXene, forming a parallel-arranged framework (PA-MXene/CNT) after freeze-drying [115]. In comparison with the random MXene/CNT host, the PA-MXene/CNT built physical barriers to block the polysulfides and enhance the chance of exposure to catalyze the conversion kinetics (Fig. 5(c)). As a result, even under a sulfur loading as high as 7 $mg \cdot cm^{-2}$, the PA-MXene/CNT@S cathode stabilized for 800 cycles at 0.5 C, exhibiting a capacity fading rate of 0.025% per cycle.

Similar to CNT, one-dimensional (1D) carbon fibers (CFs) with micrometer-scale diameter, excellent flexibility, and good conductivity are used to combine with MXenes. Wei et al. reported a sulfur host by enveloping 3D intertwined CFs with individual Ti_3C_2 nanosheets (Ti_3C_2@CF), whose structure can avoid the stack of nanosheets and significantly improve the exposure degree on the surface of MXene [72]. The CFs framework provides several holes with micrometer size and the flexible Ti_3C_2 nanosheets enveloping greatly improves the ductility of CFs. These structural features can effectively endure the stress and deformation brought from the volume expansion and prevent the pulverization of the cathode. Thus, employed with the sulfur mass loading of 4 $mg \cdot cm^{-2}$, the Ti_3C_2@CF/S cathode delivered an initial capacity of 1058.4 $mAh \cdot g^{-1}$ and retained a remarkable capacity of 624.9 $mAh \cdot g^{-1}$ after 1000 cycles at 1 C.

Apart from the 1D carbon materials of CNTs and CNFs, graphene, as a typical 2D carbon material, has also been combined with MXenes to fabricate advanced hosts for high-performance Li-S batteries. The rGO-enveloped d-$Ti_3C_2T_x$-MXene (GMr) matrix was prepared by hydrothermal and freeze-drying methods, displaying the 3D porous network structure [73]. The –COOH groups on GO and the –OH groups on d-$Ti_3C_2T_x$ MXene exchange, and then GO acts as an oxidant to partially oxidize the Ti atoms with low coordination state in d-$Ti_3C_2T_x$ MXene into TiO_2, resulting in the layered structure of d-$Ti_3C_2T_x$ MXene. On one hand, the distribution of porous structures boosts Li-ion diffusion and reduces the concentration polarization. On the other hand, the TiO_2 particles partially oxidized by $Ti_3C_2T_x$-MXene can effectively adsorb the LiPSs by increasing the polar sites on non-polar rGO surface, while the low-coordination-state Ti atoms enhance the electrochemical redox reactions of sulfur [116]. In addition to the rational designs of sulfur hosts, the shuttle effect of LiPSs can also be significantly mitigated by modifying commercial polypropylene (PP) separator with a layer of functional materials.

Table 2 A summary of MXene-based heterostructures for sulfur hosts and modifications

Heterostructure classification	Sample	Sulfur loading ($mg \cdot cm^{-2}$)	Rate	Cycle number	Capacity ($mAh \cdot g^{-1}$)	Year	Ref.
MXene-carbon heterostructures	CNT/Ti_3C_2	1.5	0.2 C	250	840	2017	[63]
	CNT/PA-MXene	7	0.5 C	800	712	2021	[71]
	Ti_3C_2@CF	4	1 C	1000	626	2020	[72]
	GO-d-$Ti_3C_2T_x$	1.5	0.5 C	1000	542.9	2021	[73]
	$Ti_3C_2T_x$/GO	—	1 C	300	575	2020	[74]
	Ti_3C_2/C	2.5	1 C	200	475	2020	[75]
	OV-T_nQDs@PCN	2.2	2 C	1000	660	2021	[76]
	MCS-SiO_2/MXene	3.2	1 C	1000	537.6	2021	[77]
	RGO/$Ti_3C_2T_x$	—	0.5 C	300	878.4	2017	[78]
	IS-MGN	2	1 C	700	764	2022	[79]
MXene-metal compounds heterostructures	V_2C/V_2O_5/CNTs	—	1 C	500	871.8	2021	[80]
	TiO_2-MXene	5.1	0.5 C	200	662	2019	[81]
	VO_x-V_2C	—	2 C	1500	441.66	2020	[82]
	VO_2(p)-V_2C	1.8	0.2 C	100	1200	2019	[83]
	V_2C/VO_2	—	5 C	500	604	2021	[84]
	1T-VS_2-MXene	1.2	2 C	500	462.9	2022	[85]
	MCCoS	—	7C	1000	468	2022	[86]
	N-MX-CoS_2	2.5	1 C	200	753	2022	[87]
	Co-$MoSe_2$/MXene	4.8	0.1 C	100	700	2021	[88]
	CoTe-MXene	2	0.1 C	250	620	2022	[89]
	MX-TiN	—	5 C	1000	516.9	2022	[90]
MXene-organic framework heterostructures	CTF/TNS	1.5	0.5 C	300	841	2020	[91]
	Ti_3C_2@iCON	—	2 C	2000	706	2021	[92]
	nMOF-867/$Ti_3C_2T_x$	1.2	0.2 C	500	624	2021	[93]
	N-Ti_3C_2/C	3.4	0.5 C	500	716	2019	[94]
	MCoNPCNs	1.5	1 C	1000	920	2019	[95]
	CoP/MXene	—	0.2 C	300	796.9	2021	[96]
	CoZn-Se@N-MX	2.9	0.1 C	100	917	2021	[97]
	N-PC/Ti_3C_2	—	1 C	800	527	2019	[98]
MXene-polymer heterostructures	MX-NF	—	1 C	1000	645	2019	[99]
	CMP-M	—	2 C	1000	550	2022	[100]
MXene-SAs heterostructures	SA-Zn-MXene	—	1 C	400	706	2020	[101]
High-entropy MXene	HE CN-MXene	—	1 C	300	738	2021	[102]

That is to say, MXene-based composites are regarded as ideal separator coating materials in Li-S batteries to further suppress the shuttle effect and promote the diffusion of lithium ions. A free-standing $Ti_3C_2T_x$/GO modified separator was synthesized by simple vacuum filtrating of the uniform dispersed solution of $Ti_3C_2T_x$ and GO [74]. The obtained $Ti_3C_2T_x$/GO hybrid modified separator not only inhibited the polysulfides shutting by forming tightly laminated microchannels and terminated groups on the $Ti_3C_2T_x$-MXene, but also increased the diffusion rate of lithium ion flux during discharging/charging process, as demonstrated by electrochemical experiments and optical and X-ray characterizations.

Besides the above-mentioned synthesis process, the MXene/carbon heterostructure can also be obtained by *in-situ* synthesis method. For example, the Ti_3C_2/C hybrid material with an expanded layer spacing ranging from 9.0 to 12.7 Å was prepared by one-step heating treatment in molten potassium hydroxide [75]. Ti_3C_2-MXene with surface terminations of –OH ($Ti_3C_2(OH)_2$) was converted to TiO_2 under heating treatment, and then TiO_2 was converted into titanate after reacting with molten KOH, which can be removed after acid washing. While the internal carbon atoms in Ti_3C_2-MXene migrate outward during the heating treatment, leaving disordered carbon layers between the MXene layers to form the Ti_3C_2/C hybrid. The residual disordered carbon in the Ti_3C_2/C heterostructures accelerates the charge transfer kinetics and provides additional deposition sites for Li_2S, endowing the obtained S cathode with ultrahigh initial discharge capacity (1668 $mAh \cdot g^{-1}$) at 0.1 C. In order to further enhance the chemisorption and catalytic conversion of LiPSs, the oxygen-vacancy-rich Ti_nO_{2n-1} quantum dots (QDs) *in-situ* uniformly distributed on porous carbon nanosheets (OV-T_nQDs@PCN) were prepared [76]. $Ti_3C_2T_x$ was treated with H_2O_2 dilution for a short time and then quenched in liquid nitrogen to oxidize Ti atoms into TiO_2 particles within the size of quantum dots, while the 2D carbon layer was retained due to the mild oxidation. Then after carbothermal reduction in H_2/Ar

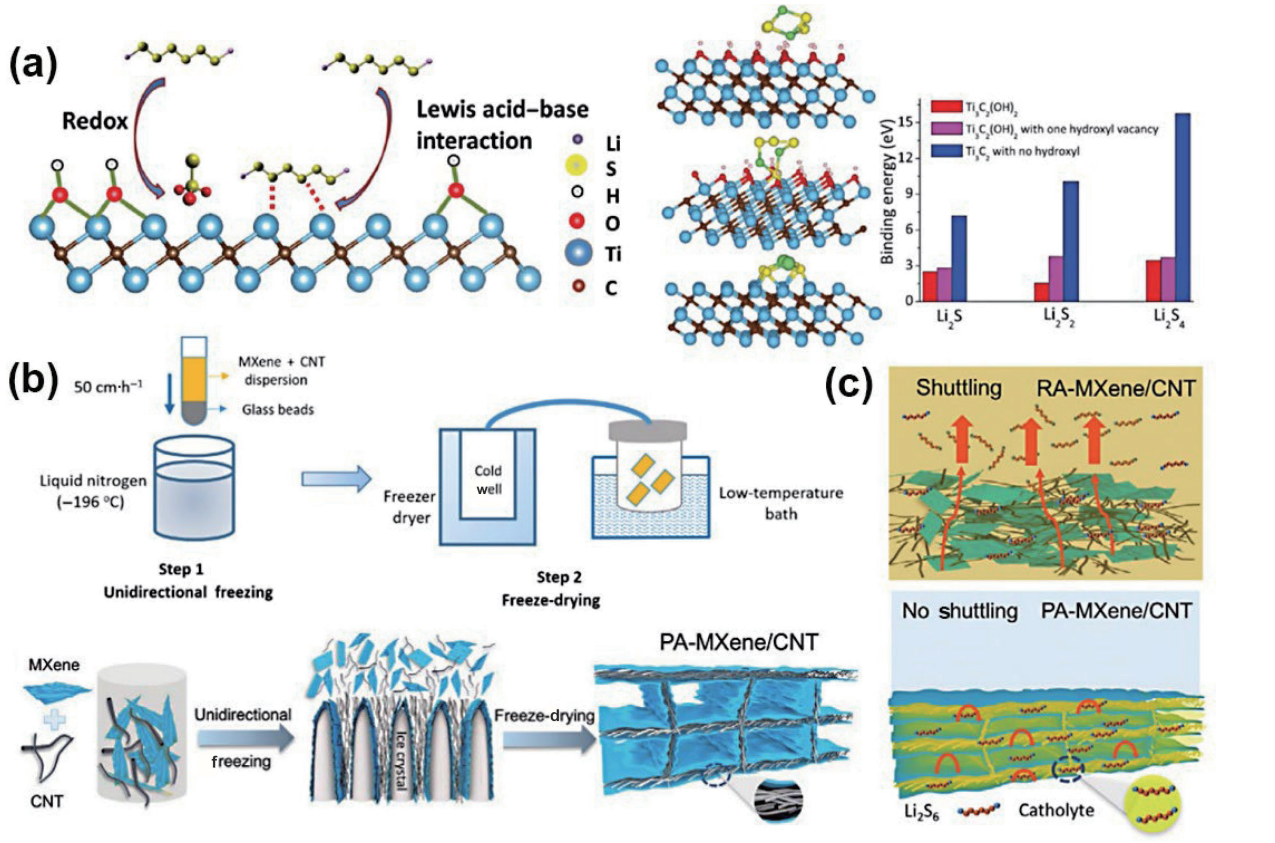

Figure 5 (a) Schematic illustration and calculations of interaction between hydroxyl decorated MXene and LiPSs. Reproduced with permission from Ref. [63], © WILEY-VCH Verlag GmbH & Co. KgaA, Weinheim 2016. (b) Schematic of PA-MXene/CNT aerogel fabrication process. (c) The schematic mechanism of Li-S batteries with PA-MXene/CNT and RA-MXene/CNT. Reproduced with permission from Ref. [71], © Wiley-VCH GmbH 2021.

atmosphere, oxygen in the lattice was detached, leaving the oxygen vacancy site, thus obtaining the OV-T_nQDs@PCN. The introduction of oxygen vacancies shortens the binding bond length between Li_2S_4 and T_nQDs, reducing the adsorption energy to further promote the immobilization and conversion of LiPSs (Fig. 6(a)). That is to say, the OV-T_nQDs act as chemical adsorption and catalytic centers to capture and reversibly transform the LiPSs. While the porous carbon sheets provide physical confinement for LiPSs and serve as substrates to prevent T_nQDs aggregation (Fig. 6(b)). Strikingly, by the aid of *in-situ* Raman, the working principle of sulfur cathode was changed and catalyzed by the OV-T_nQDs, displaying the reaction path from "$S_8 \rightarrow S_x^{2-} \rightarrow S_x^{2-} \rightarrow S^{2-}$" to "$S_8 \rightarrow S_x^{2-}$ + $S_2O_3^{2-} \rightarrow S_4^{2-}$ + $S_xO_6^{2-} \rightarrow S^{2-}$". Integrating the "catalysis, constraint and electroconductibility" into one design makes the fabricated cells display a superb long-term cycling stability with a sulfur loading of 2.2 mg·cm^{-2} under an E/S ratio of 10 μL·mg^{-1} (88% capacity retention over 1000 cycles at 2 C).

Apart from the 2D carbon materials, carbon nanosphere, as a zero-dimensional (0D) carbon material, has also been combined with MXenes to provide sufficient space to loading sulfur and accommodate volume expansion during cycles. For example, mesoporous carbon nanospheres (MCS-SiO_2) firmly embedded in the interlayer space of MXene nanosheets were prepared by the strategies of self-assembly and high-temperature pyrolysis (Fig. 6(c)) [77]. During the hybrid composite, the MCS-SiO_2 captures the polysulfides via physical confinement and alleviates the volume expansion and collapse. While the MXene nanosheets with terminal functional groups accelerate the conversions of LiPSs into Li_2S, which are furtherly proved by *in-situ* X-ray diffraction (XRD) and *in-situ* Raman (Fig. 6(d)). Taking the *in-situ* XRD as an example, the peak intensity of crystallized sulfur gradually decreases and finally transforms into Li_2S in the discharge process, while the characteristic peak of S_8 comes back in final charging stage (1.9 V). Accordingly, the synergistic effect of the MCS-SiO_2 and MXene can effectively avoid the shuttle effect, guarantee the uniform deposition of Li_2S and accelerate the diffusion of lithium-ion. Therefore, the formed sulfur cathode remained at 600 mAh·g^{-1} after cycled 1000 cycles at 1 C.

3.2 MXene-metal compounds heterostructures

Generally, to prepare high loading sulfur cathode, carbon-based composites tend to exhibit thicker structures while the metal-based matrix always possesses higher tap densities, which can further increase the volume energy density of Li-S batteries [117–119]. Combining metal compounds with MXene can enhance the chemical adsorption capability towards polysulfides and inhibit the stacking of MXene nanosheets, raising increasing attentions. At the earliest, metal oxide-MXene heterostructure served as bidirectional catalysts for liquid–solid sulfur/sulfide redox conversions. In 2019, a TiO_2-MXene heterostructure was made by partly oxidizing the pristine $Ti_3C_2T_x$ nanosheets into TiO_2 via hydrothermal treatment [81]. A coating layer with a thickness of less than 5 μm was achieved by mixing the TiO_2-MXene heterostructure with graphene. Thanks to the strong adsorption of TiO_2 to anchor polysulfides, the oxygen-sealed MXene exerts high catalytic activity to polysulfide conversions, ensuring smooth and rapid diffusion of Li ions. Thus, the fabricated cathode with TiO_2-MXene heterostructure catalyst cycled for 1000 cycles at 2 C with a capacity decay rate as low as 0.028% per cycle. Besides, a series of MO_x-MXene (M: Ti, V, and Nb) heterostructures were synthesized by one-step hydrothermal method involving etching and oxidation simultaneously (Fig. 7(a)) [82]. Despite the generation of VO_x will partially reduce to the high conductive V_2C, the VO_x-V_2C heterostructure still maintains the metallic properties as simulated in the density of states (DOS).

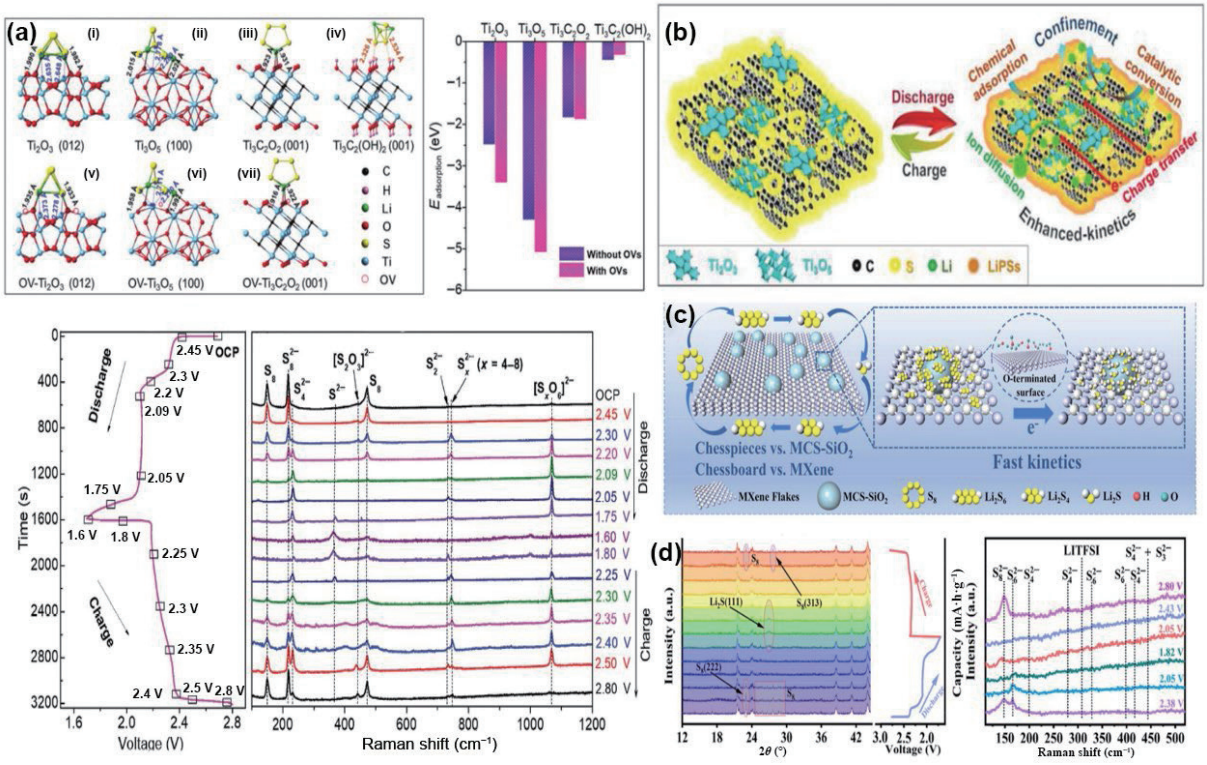

Figure 6 (a) Theoretical and experimental characterization of LiPSs chemisorption and conversion. (b) Schematic illustration of discharging/charging process of OV-T_nQDs@PCN. Reproduced with permission from Ref. [76], © Wiley-VCH GmbH 2021. (c) Schematic illustration of the conversion of LiPSs in S@MCS-SiO_2/MXene cathode. (d) *In situ* XRD patterns and *in situ* Raman spectra of S@MCS-SiO_2/MXene. Reproduced with permission from Ref. [77], © Elsevier B. V. 2021.

Meanwhile, the free energy barriers of sulfur species on the VO_x-V_2C heterostructure were comprehensively investigated, which is better than the other two counterparts (TiO_x-Ti_3C_2 and NbO_x-Nb_2C), and is more thermodynamically conducive to the reduction from S_8 to Li_2S (Fig. 7(b)). Experimental results revealed that the prepared VO_x-V_2C/S cathode outperformed the other two, exhibiting a low capacity attenuation rate of 0.027% per cycle after 1500 cycles at 2 C. Moreover, the fast ionic transport tunnel was constructed by 3D printed electrode and the high sulfur loadings of 3D printing electrodes (3DPE) were achieved by varying the printing layer numbers. Compared to the long ion transportation paths in normal coated electrode, the 3D printed VO_x-V_2C/S electrode exhibited superior cycling stability (800 mAh·g^{-1} after cycling for 100 times at 1 C) due to its hierarchical porous and conductive framework (Fig. 7(c)). Different from ordinary VO_2, VO_2(p) (paramontroseite-VO_2) is viewed as a promising room-temperature conductivity material among all VO_2 crystals [120, 121]. Via hydrothermal treatment of $NaVO_4$ and V_2C MXene, VO_2(p) nanorod clusters grow vertically on the surface of V_2C-MXene nanosheets [83]. The grid structure composed of VO_2(p) nanorod clusters can support high sulfur loading and provide a larger specific surface area to accelerate the electrochemical process. In addition, the theoretical calculation proves that VO_2(p) is a direct bandgap semiconductor, so the VO_2(p)-V_2C heterostructure composed of semiconductor and conductor produces different band dispersion near the Fermi level (Fig. 7(d)), which affects the band structure and electron transport at the interface. Furthermore, it is demonstrated that the reaction kinetics from Li_2S_2 to Li_2S is the rate-determining step in the whole redox reaction, which has the largest reaction energy barrier. The simulation results show that the sulfur species on VO_2(p)-V_2C heterostructure has lower reaction barriers (Fig. 7(e)), accelerating the conversion from LiPSs to Li_2S, especially for Li_2S_2 to Li_2S. Thus, the VO_2(p)-V_2C/S cathode retained a discharge capacity of 855 mAh·g^{-1} after 500 cycles at 2 C, corresponding to a capacity retention rate of 69.1%. Compared with the metal oxides, metal sulfides have higher electrical conductivity and catalytic properties than metal oxides, accelerating their further combination with MXene. Li et al. reported the dual-conductive 1T-VS_2-MXene heterostructure as a bidirectional electrocatalyst by one-step hydrothermal reaction (Fig. 8(a)) [85].

Compared with 2H phase VS_2 semiconductor materials, the 1T metallic phase VS_2 nanosheet possesses excellent hydrophilicity, superior electronic conductivity and abundant electrochemical reaction sites [122–124]. Combined with MXene, the unoccupied conduction band of 1T-VS_2 is occupied and shifted to the Fermi level, resulting in superior conductivity and faster lateral charge transfer. The designed heterostructure combines the merits of anchoring ability and catalytic conversion (1T-VS_2) for LiPSs with good nucleation/decomposition (MXene) of Li_2S to accelerate the bidirectional sulfur redox kinetics, which is further proved by adsorption energies between LiPSs and 1T-VS_2-MXene, to achieve balanced adsorption-catalytic and conversion-nucleation for sulfur species. Similarly, a multi-dimensional MXene@CoS_2 heterostructure as a separator coating by electrostatic interaction and hydrothermal vulcanization was prepared by Peng et al. (Fig. 8(b)) [86]. The CoS_2 facilitated the electron transfer to the Ti_3C_2-MXene surface, reducing the valence state of Ti, leading to the change of charge distribution center and the density of states. The transmission electron microscopy (TEM) image displayed an obvious crystalline boundary of the two materials (Fig. 8(c)). As shown in Figs. 8(d) and 8(e), the presence of CoS_2 can effectively reduce the reaction barrier from LiPSs to Li_2S and lower the energy barrier of Li_2S decomposition. For example, the decomposition barrier was significantly reduced from 0.46 to 0.30 eV with the aid of CoS_2. Thus, the battery with MXene@CoS_2 catalyst finally achieved a major breakthrough in rate performance at an ultra-high current density of as high as 20 C and long cycle performance up to 1000 cycles at 7 C with the attenuation rate of 0.033%.

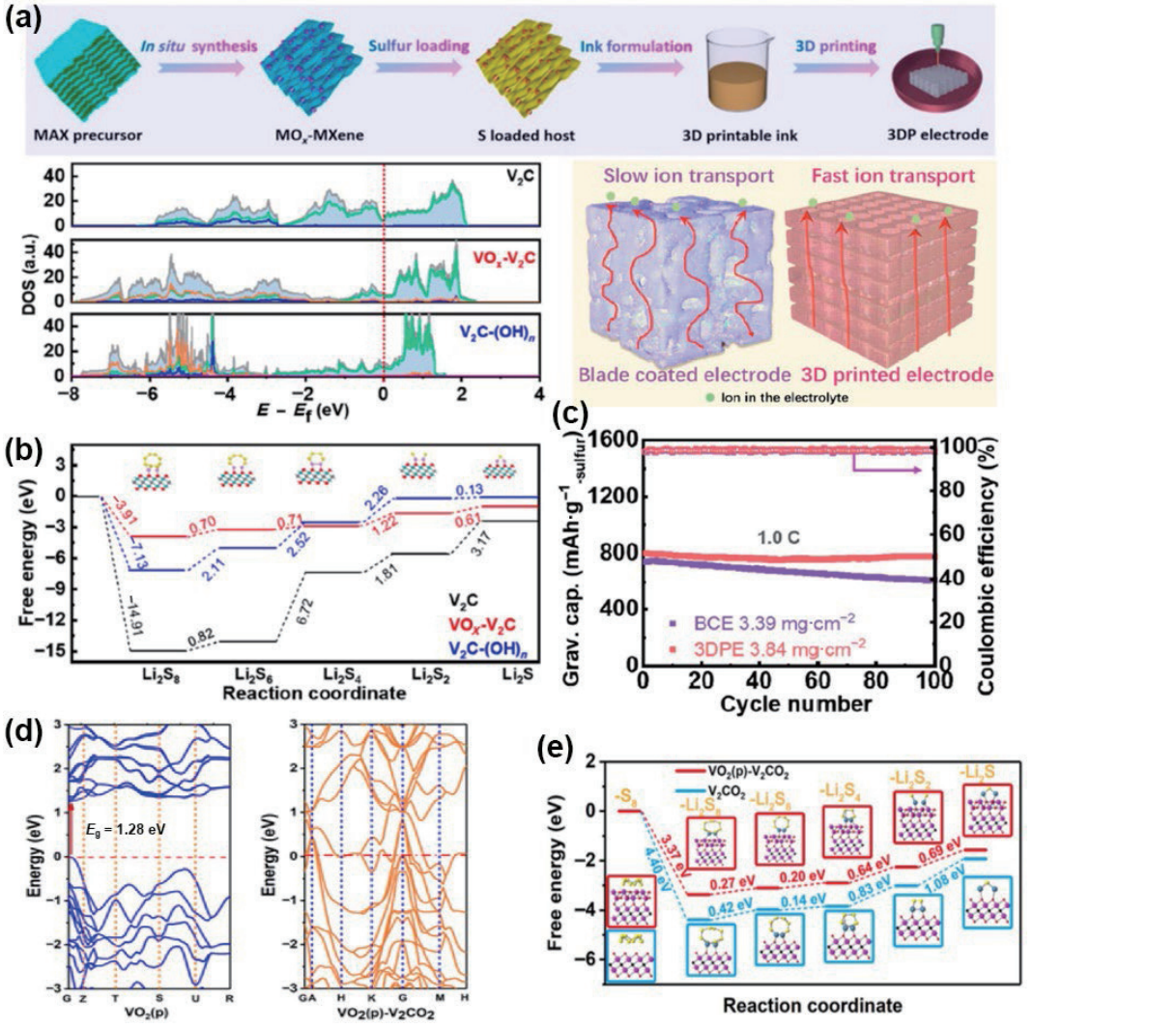

Figure 7 (a) Synthesis process of MO_x-MXene. (b) Gibbs free energies for LiPSs conversion reactions on V_2C, VO_x-V_2C and V_2C-$(OH)_n$. (c) Electrochemical performance in blade-coated electrode (BCE) and 3DPE models. Reproduced with permission from Ref. [82], © American Chemical Society 2020. (d) Energy band diagrams of VO_2(p) and VO_2(p)-V_2C. (e) Energy profiles for LiPSs on VO_2(p) and VO_2(p)-V_2C. Reproduced with permission from Ref. [83], © American Chemical Society 2019.

Another CoS_2-MXene bifunctional heterocatalytic structure was prepared by molten salt etching and sulfidation (Fig 9(a)) [87]. In the CoS_2-MXene heterostructure, the nitrogen doping sites and CoS_2 nanoparticles exert the adsorption affinity with LiPSs, while the heterogeneous CoS_2-MXene interface accelerates the decomposition process of insulated Li_2S. By taking advantage of the synergistic effect of adsorption and catalytic conversion, the Li-S batteries with N-CoS_2-MXene modified separator achieved an ultra-high initial capacity and excellent cycling stability.

Due to relatively similar electronegativity and ionic radius of S and Se, transition metal selenides exhibit similar crystal structures and polarity characteristics compared to metal sulfides [125]. However, the electronic conductivity of transition metal selenides is much higher than that of transition metal sulfides, because Se is characterized by electrical conductivities (1×10^{-3} S·m^{-1}), many orders of magnitude higher than that of S (5×10^{-28} S·m^{-1}) [126–128]. Thus, Co-$MoSe_2$/MXene heterostructure as a dual-functional catalyst was synthesized by doping cationic cobalt into $MoSe_2$ via hybridization with MXene under hydrothermal conditions (Fig. 9(b)) [88]. Research findings confirm that the introduction of Co atom forms a shorter Co–Se bond (Figs. 9(c)–9(e)), which can promote the Mo 3d band to approach the Fermi level, adjusting the electronic structure and coordination environment of $MoSe_2$, as well as increasing the disorder and defects. Thanks to the unique advantages, the Co-$MoSe_2$/MXene heterostructure provides more catalytic active sites for nucleation and dissolution of Li_2S, greatly improving the intrinsic catalytic activity and conductivity of $MoSe_2$ as simulated and tested in Figs. 9(f) and 9(g) [129]. These merits endowed the Co-$MoSe_2$@S cathode with a high reversible capacity of 1454 mAh·g^{-1} under a sulfur loading of 4.8 mg·cm^{-2} and an E/S ratio of 3.5 μL·mg^{-1} at 0.1 C.

Cobalt tellurium also has received growing attention recently due to its more metallic properties and better stability during the electrochemical processes than corresponding selenides [130–132]. Chen's group reported 1D CoTe nanorods/2D MXene heterogeneous bifunctional electrocatalysts for high operating temperature Li-S batteries (Fig. 9(h)) [89]. The Te nanorods were grown on MXene nanosheets by N_2H_4 reduction and subsequently converted to CoTe-MXene heterostructures under solvothermal conditions. This robust 1D/2D architecture design with multiple components significantly accelerates the nucleation and decomposition of Li_2S and improves the PP separator's heat resistance after composite coating. Compared with the other three separators, the modified separator can withstand high temperature rise (90 °C) without any deformation (Fig. 9(i)). Under high operating temperature environment (60 °C), the battery with CoTe-Mxene modified separator retained a high areal capacity of

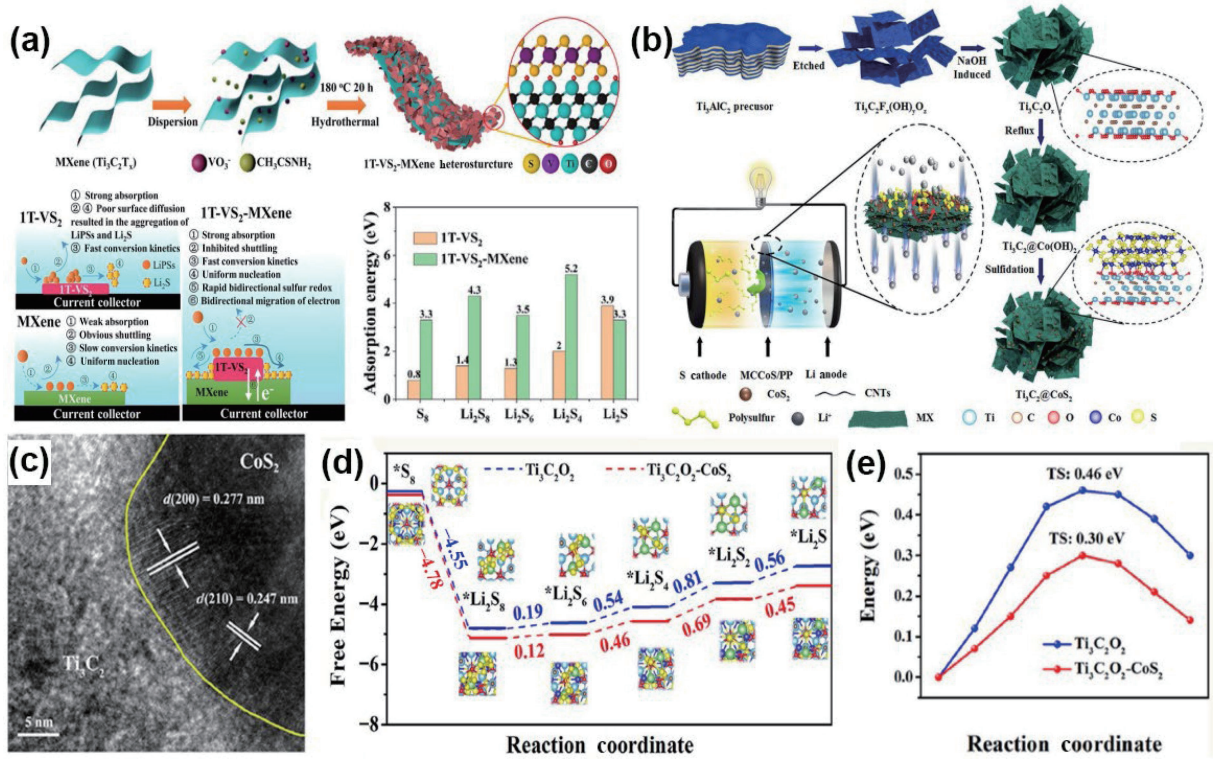

Figure 8 (a) Synthesis process, synergistic mechanism and simulated calculation of 1T-VS_2-MXene. Reproduced with permission from Ref. [85], © Elsevier B. V. 2022. (b) Schematic process illustration of MX@CoS_2. (c) high-resolution TEM (HRTEM) image of MX@CoS_2. (d) The Gibbs free energy profiles of LiPSs on $Ti_3C_2O_2$-CoS_2 and $Ti_3C_2O_2$. (e) Energy profiles of Li_2S decomposition on $Ti_3C_2O_2$-CoS_2 and $Ti_3C_2O_2$. Reproduced with permission from Ref. [86], © Tian, S. H. et al. 2022.

4.0 mAh·cm^{-2} after 50 cycles under lean electrolyte (4 μL·mg^{-1}) (Fig. 9(j)).

3.3 MXene-organic framework heterostructures

In recent years, covalent organic frameworks (COFs) have attracted much attention due to their regular structural periodicity, inherent porosity, and rich functional ligands [133, 134]. However, the electrical conductivity of COFs is far from the demand applied in batteries, which can be effectively compensated by combining with conductive MXene [135]. Yang's group reported a 2D-2D heterostructures consisting of *in-situ* grown layered porous COF on the Ti_3C_2-MXene nanosheets (Fig. 10(a)) [91]. This heterostructure delivers a surface area of 318 m^2·g^{-1} and provides large amounts of micropores and mesopores to load sulfur and tolerate the volumetric changes. Theoretical calculation and X-ray absorption near-edge structure (XANES) show that Ti_3C_2 MXene nanosheets (TNS) has stronger adsorption energy for Li_2S_6 through Ti–S bonds, while covalent triazine framework (CTF) has strong adsorption energy for Li_2S_4 through Li–N bonds (Figs. 10(b)–10(e)). Besides, a strong Ti–N bond is formed between the CTF and TNS, which induces interfacial electron transfer and interfacial mechanics. The ordered pore structure and the lithiophilic site of triazine ring N in COF, coupled with the sulfurophilic sites in Ti_3C_2, make S@CTF/TNS cathode display an excellent cycling performance. With a high sulfur content of 76%, the cathode achieved an initial capacity of 1441 mAh·g^{-1} at 0.2 C and retained a low capacity decay rate of 0.014% per cycle at 1 C. Another guanidine ion-covalent organic nanosheet (iCON) uniformly distributed on the surface of Ti_3C_2-MXene nanosheet was prepared by electrostatic and hydrogen bonding (Fig. 10(f)) [92]. The Schiff-bases condensation reaction between guanidine and phloroglucinol results in the formation of tremella-like Ti_3C_2@iCON heterostructure. The positively charged guanidine unit captures the negatively charged polysulfides by electrostatic adsorption, so as to inhibit the LiPSs migration to Li anode. Besides, the Ti_3C_2-MXene nanosheet accelerates the transformation of polysulfides and brings about the uniform nucleation/deposition of Li_2S. As a result, the synergistic effect of Ti_3C_2@iCON-PP made the battery maintain a high capacity of 1186 mAh·g^{-1} after 200 cycles at 0.1 C.

Metal-organic frameworks (MOFs), another kind of novel organic porous framework materials, have also been widely studied due to their large specific surface area, high porosity, pore size controllability, opened metal center and heteroatomic doping sites [136–138]. As reported, 3D layered Zr-MOF/$Ti_3C_2T_x$ nanosheets were prepared through an *in-situ* solvothermal method and electrostatic self-assembly [93]. The Zr-MOF with the shape of polyhedron locates in the interlayer of $Ti_3C_2T_x$-MXene nanosheet, which effectively inhibits the stacking of MXene nanosheets and fully exposes the surface active sites of MXene. During the discharging/charging process, the Zr-MOF interacts with LiPSs by forming Li–N and Zr–S bonds to inhibit the loss of active sulfur species. Besides, the unique 3D Zr-MOF/$Ti_3C_2T_x$ heterostructure possesses a large specific surface area of 911.5 m^2·g^{-1} and a pore volume of 0.36 cm^3·g^{-1}, which is beneficial to store more intermediate active materials and offer sufficient electrochemical reaction active sites.

Compared with the pristine MOF-based heterostructure materials, the derivatives from MOF/MXene heterostructure usually have a richer porous structure and heteroatom-doped composition, which is conducive to achieving better stability and electrochemical performance. For example, Li et al. reported a nitrogen-doped porous carbon modified MXene heterostructure (N-Ti_3C_2/C) by simple heating treatment under reductive 10% H_2 atmosphere and acid washing (Fig. 11(a)) [94]. Evenly distributed nitrogen heteroatoms as preferential lithium-ion transfer sites effectively promote the uniform diffusion of lithium-ion flux. The resultant battery with N-Ti_3C_2/C coated separator maintains a high and stable specific capacity (an areal capacity of 6.3 mAh·cm^{-2} after 50 cycles at 0.1 C) when the sulfur loading is over 10 mg·cm^{-2}. Similarly, a spongy shaped MXene-based

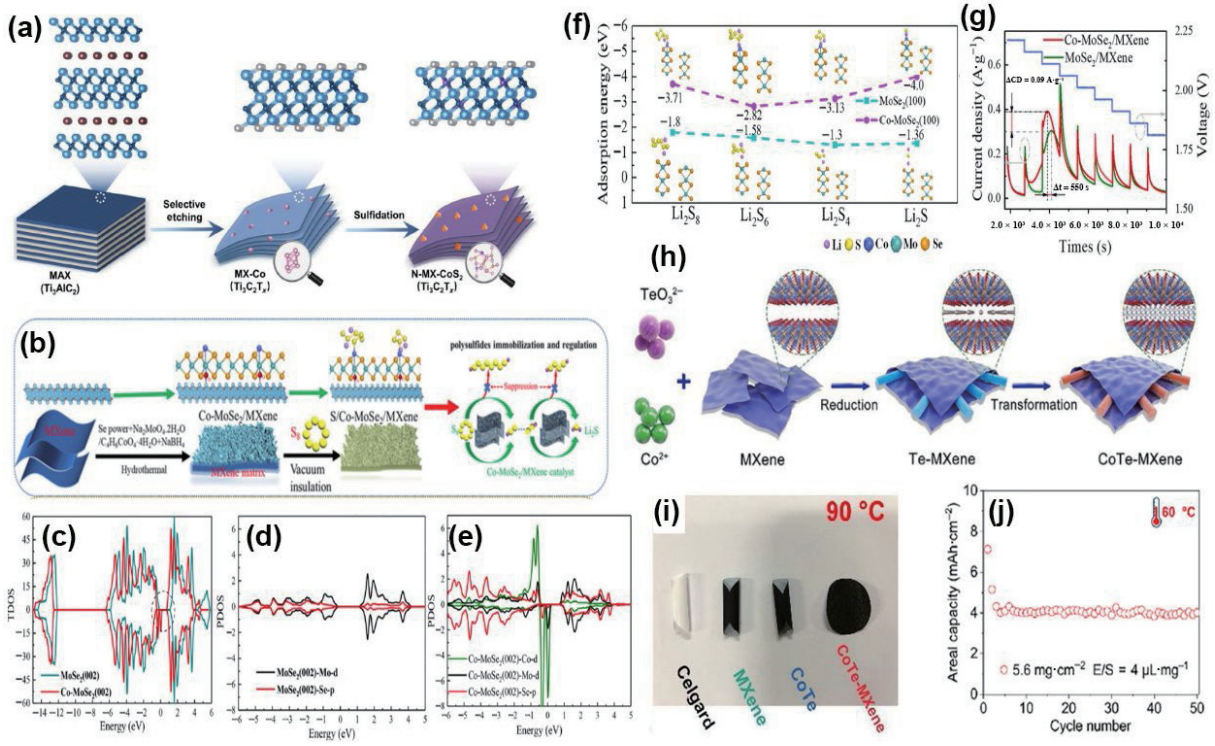

Figure 9 (a) Schematic preparation illustration of N-MX-CoS_2. Reproduced with permission from Ref. [87], © Elsevier B. V. 2021. (b) Schematic process illustration of Co-$MoSe_2$. (c) Total density of state (TDOS) plots and ((d) and (e)) projected density of states (PDOS) plots of the main orbital contribution for $MoSe_2$ and Co-$MoSe_2$. (f) Adsorption energies of the Co-$MoSe_2$/MXene. (g) Current profiles under potentiostatic intermittent titration technique (PITT) on Co-$MoSe_2$/MXene and $MoSe_2$/MXene. Reproduced with permission from Ref. [88], © American Chemical Society 2021. (h) Schematic illustration for the preparation process of CoTe-MXene. (i) Thermal endurance property of different separators under 90 °C. (j) Cycing performance of CoTe-MXene with lean electrolyte under 60 °C for 0.02 C. Reproduced with permission from Ref. [89], © Elsevier B.V. 2021.

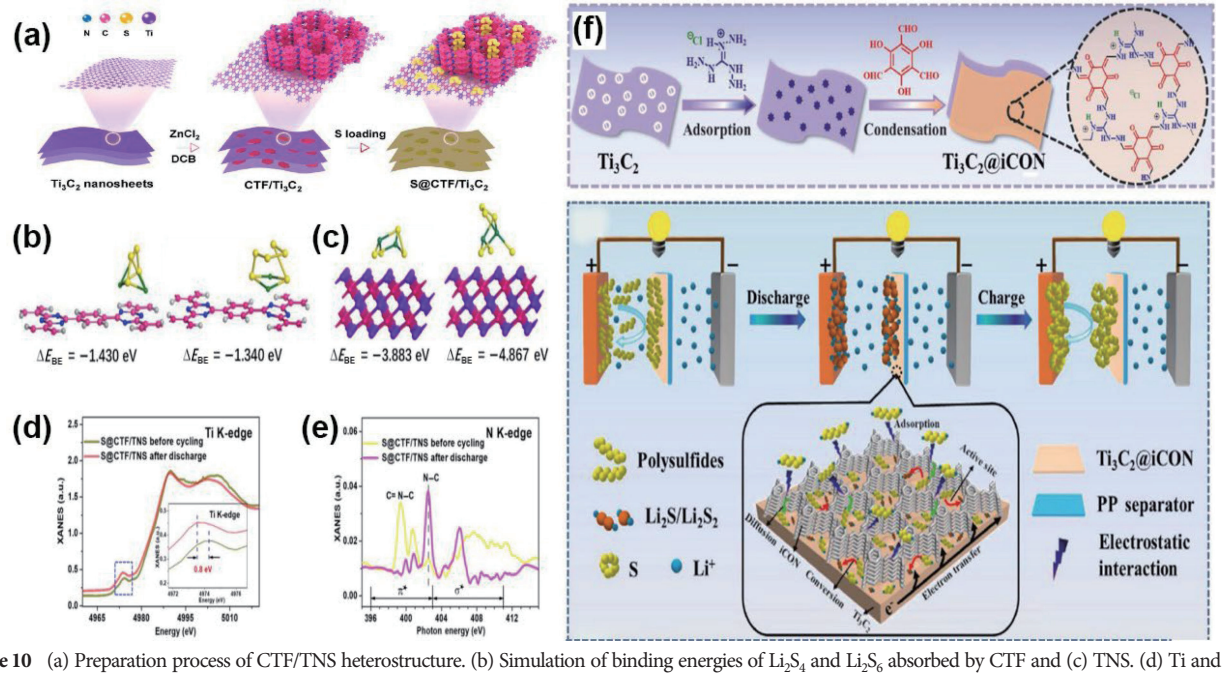

Figure 10 (a) Preparation process of CTF/TNS heterostructure. (b) Simulation of binding energies of Li_2S_4 and Li_2S_6 absorbed by CTF and (c) TNS. (d) Ti and (e) N K-edge of the S@CTF/TNS electrode before and after cycling. Reproduced with permission from Ref. [91], © Elsevier Ltd. 2020. (f) Schematic illustration process and LiPSs conversion mechanism of Ti_3C_2@iCON. Reproduced with permission from Ref. [92], © Wiley-VCH GmbH 2021.

heterostructure with Co/N co-doped porous carbon nanosheets (MCoNPCNSs) was obtained (Figs. 11(b) and 11(c)) [95]. Due to the catalytic graphitization of Co during calcination, 3D carbon nanocages are formed to encapsulate the Co, avoiding the etching of Co by HCl when removing Zn. The resultant MXene-based heterostructure possesses abundant microporous and mesoporous structures with a specific surface area up to 726.6 $m^2 \cdot g^{-1}$ and a pore volume up to 0.71 $cm^3 \cdot g^{-1}$, which confers amounts of electroactive sites and adequate room to adsorb LiPSs and accommodate sulfur. Besides, the Co/N co-doping efficiently enhances the adsorption ability of polysulfides and promotes the kinetics of sulfur redox conversion, contributing to excellent electrochemical performances.

The low temperature phosphating of Ti_3C_2/ZIF-67 was selected to realize the typical sandwiched-like structure of CoP@MXene heterostructure (Fig. 11(d)) [96]. Ti_3C_2-MXene supports a

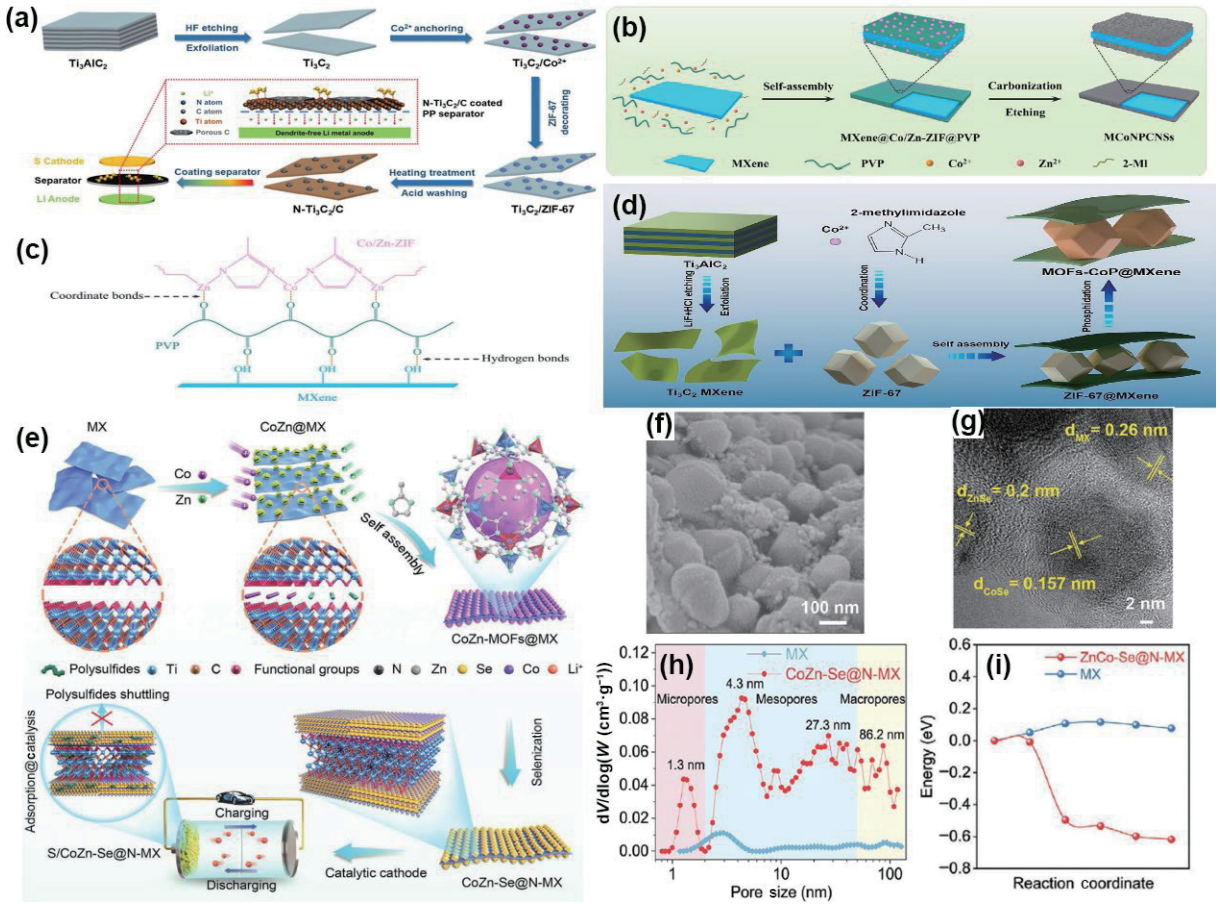

Figure 11 (a) Schematic illustration for the synthesis of N-Ti_3C_2/C nanosheets. Reproduced with permission from Ref. [94], © Elsevier B. V. 2019. (b) Schematic preparation of the MCoNPCNSs composite. (c) Schematic illustration of bonds in MXene@Co/Zn-ZIF@PVP. Reproduced with permission from Ref. [95], © American Chemical Society 2019. (d) The synthetic illustration of the MOFs-CoP@MXene. Reproduced with permission from Ref. [96], © Elsevier B. V. 2021. (e) Synthesis process illustration of CoZn-Se@N-MX. (f) SEM and (g) TEM images of CoZn-Se@N-MX. (h) Brunauer–Emmett–Teller (BET) of CoZn-Se@N-MX. (i) Energy profiles of Li_2S decomposition on CoZn-Se@N-MX and MX. Reproduced with permission from Ref. [97], © Wiley-VCH 2021.

conductive substrate while CoP grown in the interlamination of MXene nanosheets exerts the catalytic effect on polysulfide intermediates. Consequently, the unique structure of MOF-derived CoP@MXene heterostructure can be used as an efficient bifunctional catalyst to achieve stable electrochemical performance. Similarly, a 0D-2D (CoZn-Se@N-MXene) heterostructure was synthesized by *in-situ* selenization of the self-assembled CoZn-MOF on the MXene nanosheet (Figs. 11(e)–11(g)) [97]. As a catalytic substrate, Ti_3C_2-MXene nanosheets ensure rapid electron transportation and prevent the aggregation of MOF-derived selenides. The CoZn-Se@N-MXene not only preserves the 2D backbone with rich N heteroatoms on the surface but also provides unique CoZn-Se heterostructures with tunable electronic properties, resulting in hierarchical micro-meso-macropores (Fig. 11(h)). The unique double lithiophilic–sulfiphilic binding sites (Co–S and Ti–S, Li-Se, and Li–N) effectively capture and catalyze the conversion of LiPSs. As exhibited in Fig. 11(i), the CoZn-Se@N-MXene heterostructure can significantly reduce the energy barrier of Li_2S decomposition, which also confirms its inherent ability to facilitate the sulfide oxidation reaction process. Attributed to the synergistic effect provided by CoZn-Se@N-MXene heterostructure, the obtained cathode displayed remarkable cycling performance of lasting 2000 cycles at 2 C.

3.4 MXene-polymer heterostructures

Polymers are famous for their rich abundance, numerous molecular structures and definable functional groups. Specifically, polymers with rich functional groups and tunable topologies are beneficial to capture LiPSs through strong covalent bonds. In addition, the flexible framework of the polymer can satisfy high sulfur content and alleviate the volume change of sulfur cathode during the charging/discharging process. For example, the functional separator by vacuum filtration of the dispersion of $Ti_3C_2T_x$ and Nafion was reported by Huang et al. (Fig. 12(a)) [99]. As a result, MXene nanosheet orderly stacks during the filtration process with the help of Nafion binder. Furthermore, the uniform interlayer embedding of Nafion into MXene serves as a cation permselective role—promoting the transport of Li^+, restricting the migration of LiPSs to anode through electrostatic repulsion. As mentioned above, the lamellar Nafion-MXene integrates "cationic selectivity, physical constraint and LiPSs reutilization" all in one, which exhibits outstanding electrochemical properties. Another 2D-2D sandwich-like structured sulfur host was successfully prepared by *in-situ* polymerizing a conjugated microporous polymer on bromophenyl functionalized MXene nanosheets (CMP-M, Figs. 12(b) and 12(c)) [100]. Brominated MXene acts as a template in the polymerization reaction, making the CMP-M appear in a flake shape without aggregation (Figs. 12(d) and 12(e)). The obtained CMP-M heterostructure features a sandwich structure consisting of a conductive inner layer (MXene) and two porous outer layers (CMP). On the other hand, heteroatoms in the triazine and benzothiophene units of CMP endow it with rich chemisorption sites to capture LiPSs. Based on the above synergistic effects, the S@CMP-M cathode delivered outstanding electrochemical stability including a high specific capacity of 1402 mAh·g^{-1} at 0.1 C and a low capacity decay rate of 0.025% per cycle at 2 C.

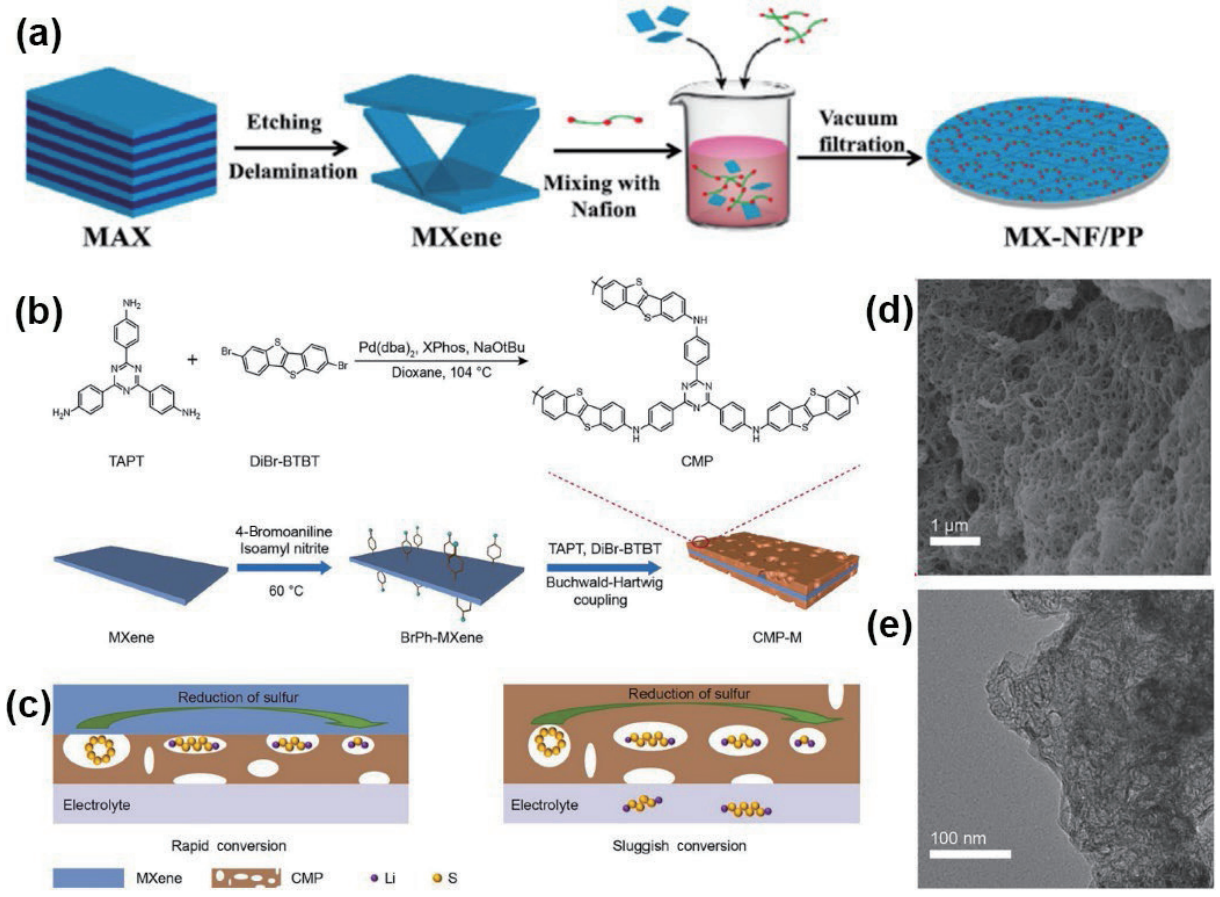

Figure 12 (a) Synthesis procedure of MX-NF/PP. Reproduced with permission from Ref. [99], © Elsevier Ltd. 2019. (b) Synthesis illustrations of CMP and CMP-M. (c) Schematic of polysulfides conversion in cathodes. (d) SEM and (e) TEM images of CMP-M. Reproduced with permission from Ref. [100], © Elsevier B. V. 2022.

3.5 MXene-single atoms (SAs) heterostructures

SAs are endowed with high exposure active centers and maximum atomic utilization, which can be served as centers of anchoring and electrocatalytic towards LiPSs [139–142]. However, single atoms easily aggregate into nanoclusters because of the high surface energy and thermodynamic instability [143–145]. Loading SAs on defect-rich MXene by strong bonding can effectively solve the agglomeration problem, maximizing the catalytic ability. Yang et al. introduced the single atomic Zn onto the Ti_3C_2-MXene surface by Lewis acid molten salt method and mixed it with sulfur spheres in an aqueous solution to obtain SA-Zn-MXene coated sulfur (S@SA-Zn-MXene) [101]. The high-angle annular dark-field scanning transmission electron microscopy (HAADF-STEM) image in Fig. 13(a) demonstrated the presence of Zn atoms highly dispersed on the Ti_3C_2-MXene nanosheet as circled. The SA-Zn-MXene layer with abundant single-atom active centers not only has good affinity with polysulfides, but also can significantly reduce the conversion free energy from Li_2S_2 to Li_2S, consequently catalyzing the conversions of polysulfides and accelerating the rate of redox reaction (Figs. 13(b) and 13(c)). In addition, the injection of atomic Zn widens the DOS around the Fermi level, causing the increase of the valence band level, which favors the excitation of electrons in SA-Zn-MXene (Fig. 13(d)). Furthermore, evenly dispersed Zn single atoms can promote the nucleation kinetics of Li_2S_2/Li_2S on the surface of MXene. Different from the traditional melt-diffusion method, the SA-Zn-MXene wrapped sulfur spheres were obtained by aqueous mixing via the strong interaction between SA-Zn-MXene and sulfur (Figs. 13(e) and 13(f)). Consequently, the S@SA-Zn-MXene cathode performed a low overpotential (~ 23 mV), a high initial capacity (1136 $mAh{\cdot}g^{-1}$ at 0.2 C), an excellent rate capacity (640 $mAh{\cdot}g^{-1}$ at 6 C) and a stable capacity with an ultralow retention rate of 80% after 200 cycles at 4 C.

3.6 High-entropy MXenes

In recent years, high-entropy metal compounds, a special kind of heterostructure, have attracted significant attention in the catalytic field due to their unique electronic structures and tunable chemical compositions. High-entropy metal compounds are solid-soluble from five or more metallic elements with similar atomic ratios, which not only make them inherit the advantages of various components but also endow them with unique properties such as lattice distortion effect, 'cocktail' effect, and slow diffusion effect. In addition, the high-entropy metal compounds have highly exposed atomic environments and abundant edge active sites, which can provide high electrocatalytic activity to drive the sulfur redox reaction. Inspired by this, Yang et al. innovatively synthesized the high-entropy carbonitride MAX phase by metallurgical treatment of the medium entropy MAX phase with other MAX phases, and further etched it in the LiF/HCl solution to obtain the high-entropy carbonitride MXene (HE CN-MXene) [102]. As shown in Fig. 13(g), the transition metal atoms of different sizes are randomly arranged and uniformly distributed in the atomic layer. Due to the lattice distortions caused by the atom difference, strong mechanical strain is created both in e_{xx} and e_{xy} directions (Figs. 13(h) and 13(i)). Benefiting from the strong mechanical strain and rich M–N bonds, the high-entropy carbonitride MXene exhibited significantly improved adsorption and catalytic ability towards polysulfides for high performance.

4 MXene-based heterostructures for dendrite free lithium anode

The high-capacity lithium metal anode suffers from the crack of solid electrolyte interphase and the dendrite formation. In order to

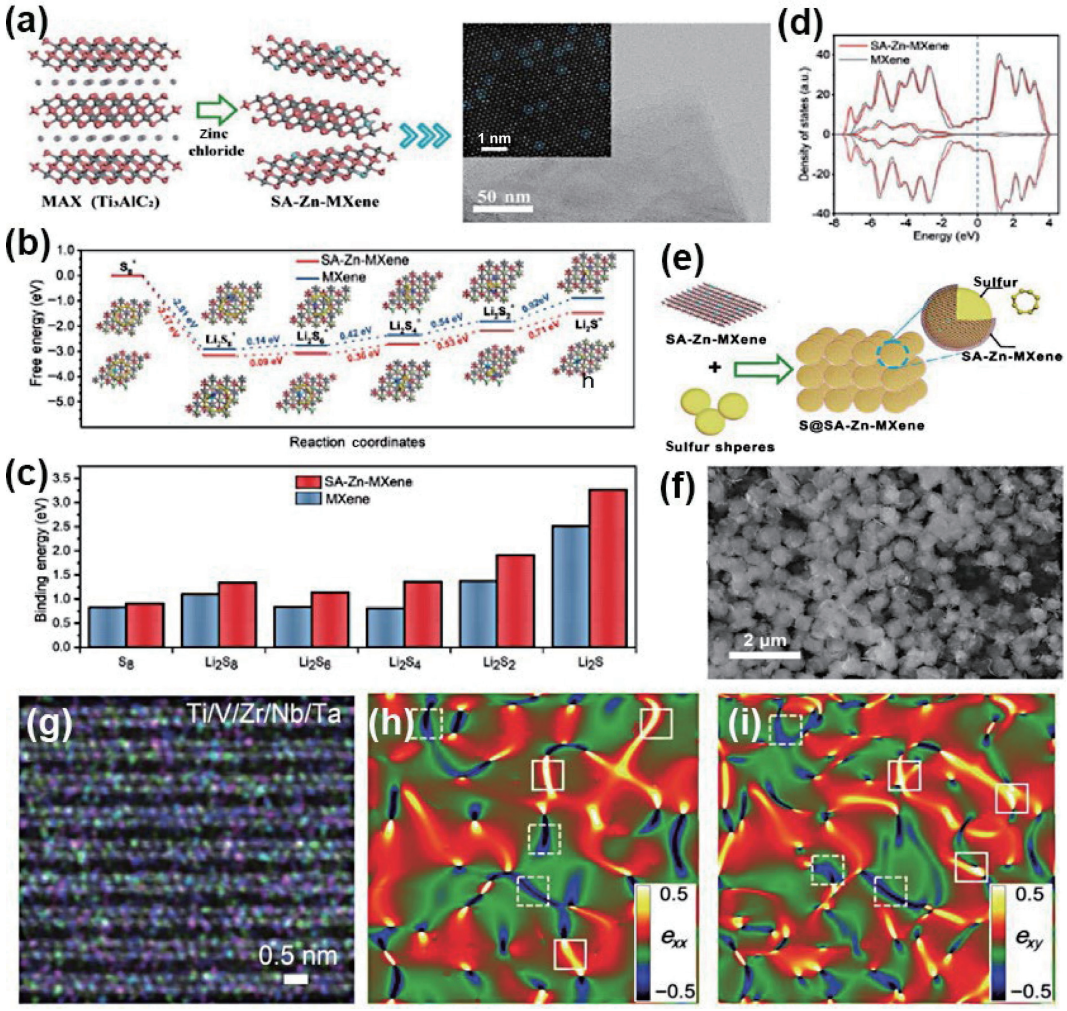

Figure 13 (a) The preparation illustration and HAADF-STEM image of SA-Zn-MXene. (b)–(d) Electrocatalytic function and the affinity to polysulfides of SA-Zn-MXene confirmed by density functional theory (DFT) calculations. (e) Fabrication illustration and (f) SEM image of S@SA-Zn-MXene. Reproduced with permission from Ref. [101], © WILEY-VCH Verlag GmbH & Co. KGaA, Weinheim 2020. (g) Overlapped atomic-resolution elemental mapping image. Strain distribution images along (h) e_{xx} and (i) e_{xy} of HE CN-MXene. Reproduced with permission from Ref. [102], © Wiley-VCH GmbH 2021.

overcome the dendrite growth problem of lithium anodes, several strategies have been proposed, including preparing a stable 3D conductive host for lithium to promote uniform lithium deposition with reducing the deposition current density; constructing stable and uniform SEI films via *in-situ* growth on liquid electrolyte additives or artificially coating, exploring suitable substrates to guide the nucleation and growth of lithium [146–151].

Acting as the lithium host, MXene shows the merits in the following aspects: (i) high conductivity and fast ionic diffusion coefficient can achieve fast electrochemical reaction during charge and discharge process to inhibit the dendrite growth; (ii) feasible structure designs with other materials into 3D porous hybrid materials can alleviate the volume expansion problem [152]; (iii) the functional groups on the surface of MXene have a certain degree of lithiophilicity, inducing uniform distribution of lithium ion flux and achieving high lithium loading. As mentioned above, MXene often faces a serious re-stacking problem during the preparation process, which greatly affects its performance and wide application [153, 154]. Therefore, assembling MXene with other materials can also make a difference in the protection of Li anode [155]. Considering these issues, the integrations of $Ti_3C_2T_x$-MXene as a 3D host have been widely used to inhibit the dendrite growth by obtaining lower local current densities [156]. A flexible $Ti_3C_2T_x$-MXene@cellulose nanofiber paper was fabricated by spin steaming technique, serving as a lithium host (Fig. 14(a)) [153]. Firstly, the MXene nanosheets formed lamellar micelles with cellulose nanofibers through hydrogen bonding. Then, under the action of roller granulation, the lamellar micelles formed spherical micelles layer by layer, resulting in nanofiber microspheres between MXene@cellulose. The interlocks between MXene nanosheets and nanofiber microspheres not only greatly improved the toughness and flexibility of films, but also prevent the re-accumulation of MXene. Besides, MXene nanosheets with functional groups showed good affinity to Li, where the –OH and –COOH groups reacted with Li, while the –F groups bound with Li by physical absorption action. MXene with –F groups exhibited stronger interactions between F and Li atoms, displaying higher binding energy (−2.70 eV) than pure MXene (−2.47 eV). With the above merits, the obtained MXene@cellulose/Li anode achieved uniform Li nucleation and growth with an overpotential of 60 mV at 1 mA·cm^{-2} over 250 cycles and a cycle time of over 1300 h at 0.5 mA·cm^{-2}. Another independent 3D structured MXene/GO (MGO) aerogel for lithium deposition via freeze-drying was fabricated (Figs. 14(b) and 14(c)) [157]. The 3D MGO framework features a high specific surface area (259 m^2·g^{-1}), light weight (3.9 mg·cm^{-3}) and interconnected pore structure, which can achieve a high lithium loading (92%) and mitigate large lithium volume fluctuations. In addition, the lithiophilicity sites in MXene nanosheets provide nucleation sites for lithium and induce uniform lithium growth (Figs. 14(d) and 14(e)). The resultant MGO-based Li anode assembled Li-S battery achieved high

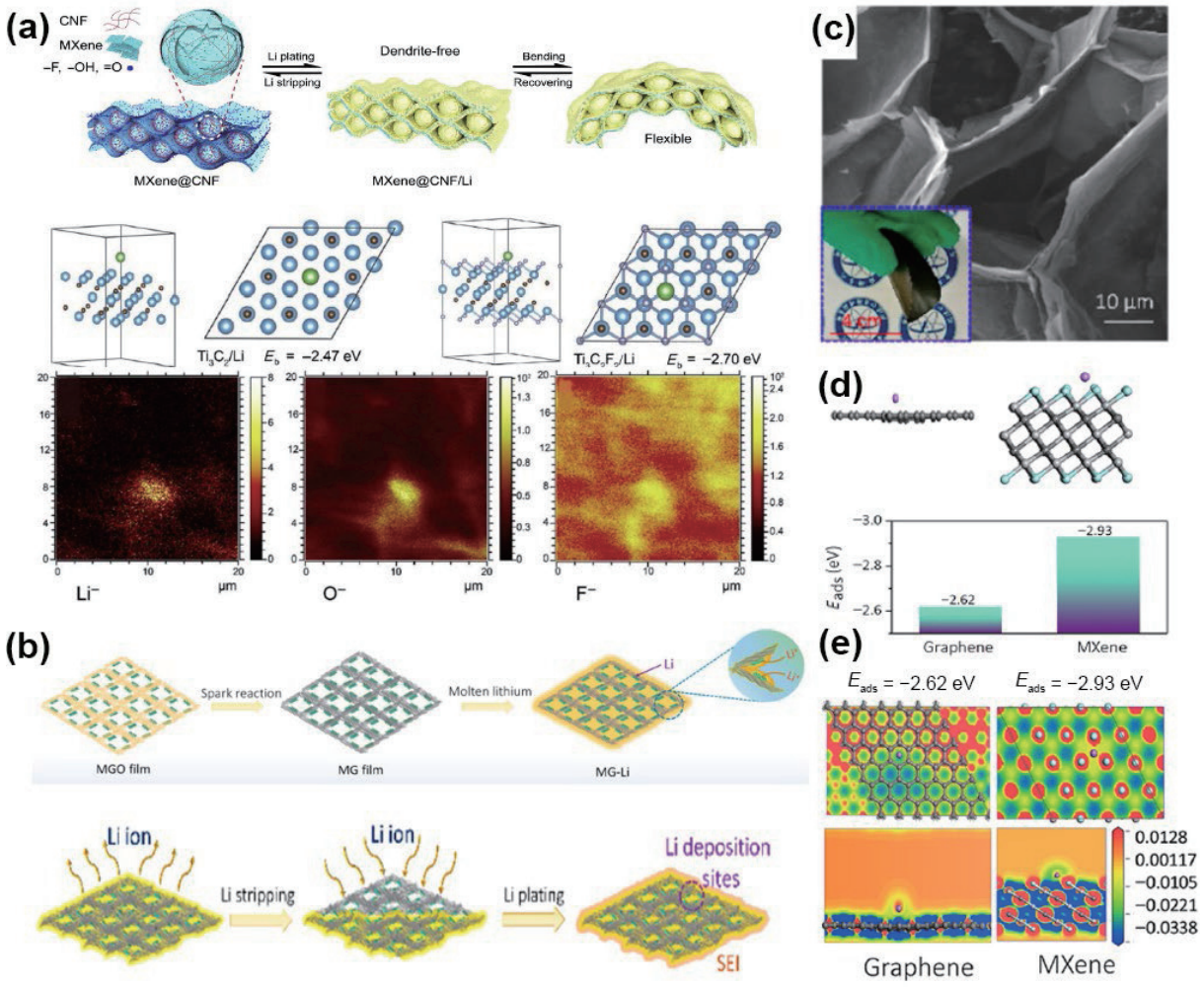

Figure 14 (a) Schematic illustration and simulated calculation of lithium plating on MXene@CNF film. Reproduced with permission from Ref. [153], © Elsevier Ltd. 2020. (b) Schematic synthesis and Li plating/stripping mechanism of 3D MG-Li anode. (c) SEM image of the MG film. (d) Binding energy of a Li atom with graphene and MXene. (e) Deformation charge density at a Li atom adsorption site of graphene and MXene. Reproduced with permission from Ref. [157], © American Chemical Society 2019.

cycling stability (a long lifespan up to 2700 h at a high capacity of 5 mAh·cm^{-2}).

Different from freeze-drying, hydrothermal treatment can be used to prepare a 3D porous MXene/rGO aerogel [152]. More abundant nucleation centers and good ion transport paths are created with the increased Ti_3C_2 content. As a result, the MXene/rGO aerogel with 3D porous structure and metal conductivity achieved fast Li-ion transport to ensure uniform plating/stripping of dendrite-free Li metal anode (Fig. 15(a)). However, these 3D open channels may also worsen the reaction of LiPSs with Li anodes. Thus, Yang et al. prepared a 2D layered structure of rGO/$Ti_3C_2T_x$ composite by vacuum filtration method to block the LiPSs and protect Li anode (Fig. 15(b)) [158]. The interface between $Ti_3C_2T_x$ and rGO has a strong adsorption effect on Li, which can guide Li nucleation/deposition uniformly and inhibit the LiPSs shutting to Li anode. The composited Li anode exhibited dendrite-free Li deposition and promoted highly reversible Li electroplating/stripping behaviors. As a result, the resultant composited Li anode exhibited superb cyclic stability over 1000 h at an ultra-high rate (10 mA·cm^{-2}) and a high area capacity (3 mAh·cm^{-2}). Another typical 2D/2D lithiophilic layer is designed as the artificial SEI for lithium anode by Gong et al. (Fig. 15(c)) [159]. The heterostructure was self-assembled in the solution of MXene and dicyandiamide by hydrogen bond and subsequently annealed to *in-situ* form the g-C_3N_4 coating on MXene. They further analyzed the SEI composition by X-ray photoelectron spectroscopy (XPS) with argon ion sputtering (Fig. 15(d)). With the increase of argon sputtering time, Li_3N and LiF became the main components of the SEI inner layer. The formation of the Li–N bond was mainly attributed to the strong interaction between Li and the N element in g-C_3N_4. These results proved that g-C_3N_4 participated in SEI formation, which inhibited the decomposition of electrolyte and regulated the uniformity of Li plating/stripping. The amorphous g-C_3N_4 makes the artificial SEI film highly homogenous to protect Li anode from continuous corrosion; abundant nitrogen species in g-C_3N_4 regulate the uniform lithium-ion flux on the electrode and reduce the nucleation overpotential, while MXene provides sufficient lithiophilic sites for Li nucleation. Consequently, the battery with MXene/g-C_3N_4@Li anode exhibited a capacity retention of 85.5% after 320 cycles at 0.5 C.

Another 2D-2D MXene@COF heterostructure was reported as the Li host [160]. The COF layer grew on aminated MXene nanosheets by Schiff base condensation under the action of an acetic acid catalyst. The growing COF layer provided not only abundant nanochannels, but also constructed layered porous scaffolds by inhibiting the re-accumulation of MXene. As a result, the Li^+ migration barrier (0.36 eV) along the lithiated COF channels was lower than MXene (0.58 eV), which can promote fast Li^+ migration (Figs. 15(e) and 15(f)). The full battery assembled with MXene@COF/Li anode achieved dendrite-free and fast charging, which had a capacity of 780 mAh·g^{-1} after 150

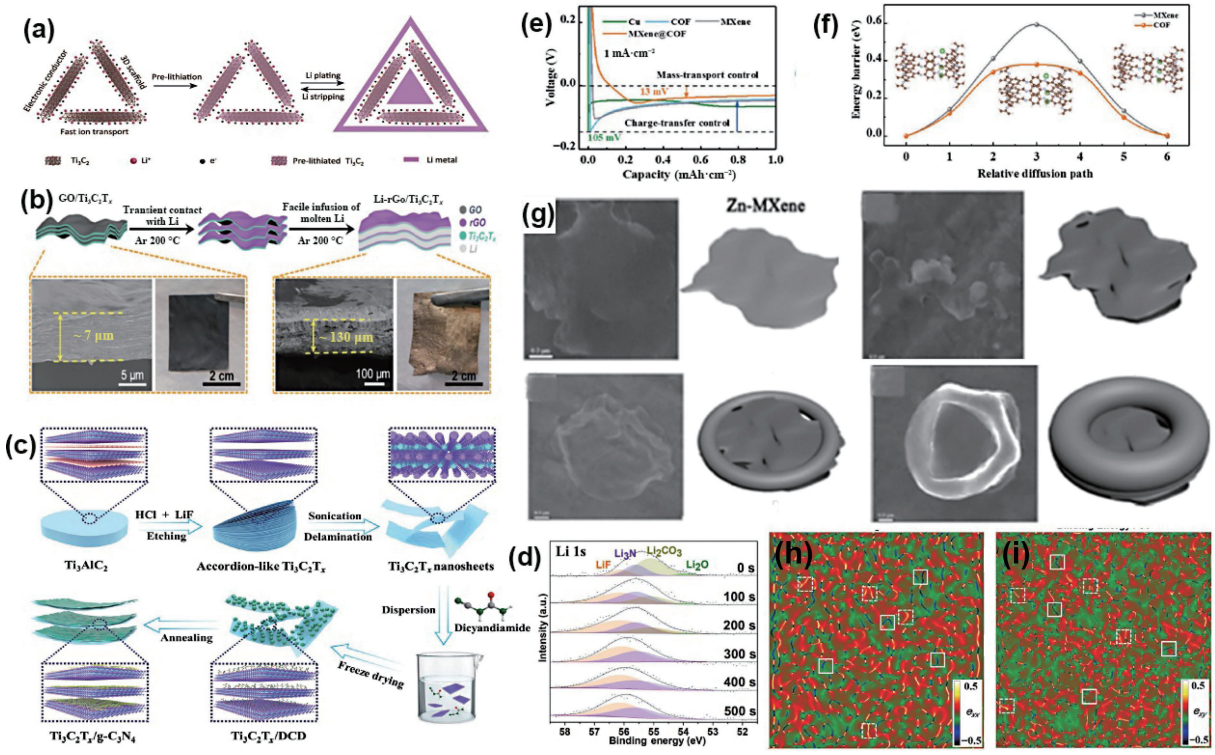

Figure 15 (a) Plating/stripping process of Li in MXene scaffold. Reproduced with permission from Ref. [152], © Wiley-VCH Verlag GmbH & Co. KGaA, Weinheim 2018. (b) Preparation process of Li-rGO/$Ti_3C_2T_x$ anode and corresponding SEM images. Reproduced with permission from Ref. [158], © Wiley-VCH Verlag GmbH & Co. KGaA, Weinheim 2020. (c) Schematic illustration process of $Ti_3C_2T_x$/g-C_3N_4. (d) Li 1s XPS depth profiles of $Ti_3C_2T_x$/g-C_3N_4 after depositing. Reproduced with permission from Ref. [159], © Zhao, F. F. et al. 2022. (e) Voltage–capacity profiles of Li deposition on MXene@COF electrodes. (f) Theoretical simulation of Li-ion migration energy diagrams for $Ti_3C_2T_x$ and in COF-LZU1 channels. Reproduced with permission from Ref. [160], © Wiley-VCH GmbH 2021. (g) Nucleation and growth diagram of Li on Zn-MXene. Reproduced with permission from Ref. [168], © American Chemical Society 2020. (h) Strain distribution of e_{xx} and (i) e_{xy} for HE-MXene. Reproduced with permission from Ref. [169], © Wiley-VCH GmbH 2021.

cycles at 0.5 C. Besides, Feng et al. also reported the successful achievement of a stable, dendrite-free Li metal anode by designing a flexible, self-supporting MXene/COF backbone for Li metal, demonstrating great application prospects [161].

Besides, metal atoms (Au, Ag, Zn) dispersed in conductive substrates can construct a lithophilic site and maximize atomic efficiency, which has been proved to be highly efficient nucleating agents and a promising strategy to produce dendrite-free lithium anodes [162–167]. Therefore, the combination of MXene with metal atoms is expected to control lithium plating behaviors. A large number of zinc atoms were substituted for Ti by the reaction of MAX with Lewis acid molten salt of $ZnCl_2$ to obtain Zn-MXene, followed by simple rolling spraying to get uniform Zn-MXene nanosheet films [168]. Due to the rich zinc atoms in the MXene layer, metallic lithium tends to uniformly nucleate on the surface of the Zn-MXene layer and grow vertically along the nucleation position to form lithium spheres. Besides, Li will grow at the edge and eventually form bowl-shaped lithium because of the strong electric field at the edge (Fig. 15(g)). As a result, dendrite-free Li anode with low overpotential (11.3 mV) and long cycle life (1200 h with an areal capacity of 1 mAh·cm^{-2}) were obtained.

In addition, high-entropy MXene also reveals great promise in inducing Li nucleation and suppressing the growth of lithium dendrites to catalyze the sulfur redox reaction. Yang et al. successfully prepared new high-entropy MXene nanosheets by selectively etching high-entropy MAX phase of $(Ti_{1/5}V_{1/5}Zr_{1/5}Nb_{1/5}Ta_{1/5})_2AlC$, where the five transition metal atoms are homogeneously formed into an MX plate in the form of solid solution phase [169]. Based on the entropy stabilization principle, the obtained high-entropy MXene atomic layer exhibited high stability and significant lattice distortion, which resulted in reinforced mechanical strain (Figs. 15(h) and 15(i)). Profiting from the strong mechanical strain and rich –F groups in high-entropy MXene, the modified lithium anode delivered an ultra-long cycling life (1 mAh·cm^{-2}, 1200 h) and deep stripping-plating behaviors (20 mAh·cm^{-2}, 500 h).

5 Summary and prospects

This review introduces and summarizes the recent advances in the design and construction of MXene-based heterostructures in Li-S batteries. Firstly, the potential of MXene and properties of MXene-based heterostructures in Li-S batteries are analyzed. Then, the functional mechanisms of the MXene-based heterostructures for sulfur cathode and lithium anode are described in detail. Specifically, MXene-based heterostructures are discussed by categorizing recent studies into six main categories: MXene/carbon heterostructure, MXene/metal compounds heterostructure, MXene/organic framework material heterostructure, MXene/polymer heterostructure, MXene/SA heterostructure, and special high-entropy MXene heterostructure. The intrinsic properties of MXene and synergistic effect of heterostructure can be utilized best: the LiPSs shuttling is greatly inhibited, and the utilization rate of sulfur is improved even under high sulfur loading, thus obtaining high discharge capacity, favorable rate performance, and cycle stability. By fully using inherent properties and controllable surface chemistry of active materials, heterostructure engineering shows great potential and prospects, providing infinite possibilities for developing high-performance Li-S batteries. After about 60 years of development, Li-S batteries have made great strides in basic research on electrocatalysts, especially in the past decade. However, some problems need to be noticed and solved to promote its large-scale commercial application in the future.

(i) Probing adsorption and conversion mechanisms of MXene-based heterostructures in Li-S batteries by *in-situ* tools

Li-S batteries' charge and discharge intermediates are complex, and detecting the interaction and influencing factors between MXene-based heterostructures and intermediates is difficult. Therefore, it is challenging to thoroughly understand the mechanisms of the adsorption and catalytic transformation of LiPSs by MXene-based heterostructures. It is also an important research field to determine active species' changes, structural evolution, and catalytic mechanisms under reaction conditions by *in situ* characterization techniques and theoretical calculations.

(ii) Developing and looking for new strategies to stabilize MXene-based heterostructures

MXene is the largest 2D material family, with more than 100 stoichiometric phases. Only about 30 kinds of MXene materials have been synthesized, and $Ti_3C_2T_x$ is the most studied in MXene, which is easily oxidized when exposed to air and water. Therefore, exploring new MXene species and heterostructures to achieve a higher stability and electrochemical performance is also a promising research field.

(iii) Binding information between MXenes and others through simulation method

The heterostructure is similar to composite material in composition, but special attention should be paid to the inherent characteristics of the component block, such as band structure, carrier density, and Fermi level difference; it should study their influence on the electronic structure and electric field distribution of the whole material as well. Besides, some unique microstructural factors of heterogeneous interfaces, such as the location and size of heterogeneous interfaces, are still unknown to ion transfer kinetics. An in-depth understanding of these fundamental and structural properties can provide theoretical guidance for constructing MXene-based high-performance heterostructures.

(iv) The catalysis evaluation of MXene-based heterostructure in large areal sulfur cathode

The most reported MXene heterostructure is evaluated in coin-cells, and excessive lithium metal is always used in the Li-S batteries. The practical application of large-scale Li-S batteries should consider more comprehensive factors, not only constrained by the structure design of sulfur cathode, separator, and lithium anode but also consider the electrochemical performance in high sulfur content, low E/S ratio, limited lithium content and different operating temperatures. In addition, attentions must be paid to the materials synthesis adapted to large-scale practical pouch cell production.

(v) More focuses of MXene-based heterostructures in lithium anode and full Li-S batteries

The application of MXene-based heterostructures in lithium anode at present is still in its early stage. In addition to being used as the host of lithium metal, MXene-based heterostructure can also be used to construct an artificial SEI layer. Combined with the advantages of MXene and other materials, it can be integrated into the artificial SEI layer to prevent contact between lithium metal and polysulfides to reduce side reactions, inhibit the growth of lithium dendrites on the surface and stabilize the lithium anode. Besides, future researches should consider the positive and negative electrode ratio of full batteries to obtain a higher energy density. In view of the aforementioned challenges and opportunities for improvement, there is still a lot of research value in MXene-based heterostructure engineering. Thanks to the functionality of MXene-based heterostructures, we believe it is a promising strategy to realize high-performance Li-S batteries in future practical applications.

Acknowledgements

This work was financially supported by the National Key R&D Program (No. 2021YFA1201503), the National Natural Science Foundation of China (Nos. 22075081, 21972164, and 22279161), the Fundamental Research Funds for the Central Universities (No. JKD01231701), and the Natural Science Foundation of Jiangsu Province (No. BK 20210130). Dr. J. Wang thanks to the fellowship awarded by the Alexander von Humboldt Foundation. Dr. Y. Zhang thanks the Shanghai Super Postdoctoral Incentive Program.

References

[1] Armand, M.; Tarascon, J. M. Building better batteries. *Nature* **2008**, *451*, 652–657.

[2] Hao, J. C.; Zhuang, Z. C.; Hao, J. C.; Cao, K. C.; Hu, Y. X.; Wu, W. B.; Lu, S. L.; Wang, C.; Zhang, N.; Wang, D. S. et al. Strain relaxation in metal alloy catalysts steers the product selectivity of electrocatalytic CO_2 reduction. *ACS Nano* **2022**, *16*, 3251–3263.

[3] Hao, J. C.; Zhuang, Z. C.; Hao, J. C.; Wang, C.; Lu, S. L.; Duan, F.; Xu, F. P.; Du, M. L.; Zhu, H. Interatomic electronegativity offset dictates selectivity when catalyzing the CO_2 reduction reaction. *Adv. Energy Mater.* **2022**, *12*, 2200579.

[4] Yin, W. N.; Cai, Y. T.; Xie, L. B.; Huang, H.; Zhu, E. C.; Pan, J. N.; Bu, J. Q.; Chen, H.; Yuan, Y.; Zhuang, Z. C. et al. Revisited electrochemical gas evolution reactions from the perspective of gas bubbles. *Nano Res.*, in press, https://doi.org/10.1007/s12274-022-5133-5.

[5] Li, S. D.; Zhuang, Z. C.; Xia, L. X.; Zhu, J. X.; Liu, Z. A.; He, R. H.; Luo, W.; Huang, W. Z.; Shi, C. W.; Zhao, Y. et al. Improving the electrophilicity of nitrogen on nitrogen-doped carbon triggers oxygen reduction by introducing covalent vanadium nitride. *Sci. China Mater.* **2023**, *66*, 160–168.

[6] Zhuang, Z. C.; Li, Y.; Li, Y. H.; Huang, J. Z.; Wei, B.; Ren, Y. J.; Ding, J.; Zhu, J. X.; Lang, Z. Q.; Moskaleva, L. V. et al. Atomically dispersed nonmagnetic electron traps improve oxygen reduction activity of perovskite oxides. *Energy Environ. Sci.* **2021**, *14*, 1016–1028.

[7] Kwade, A.; Haselrieder, W.; Leithoff, R.; Modlinger, A.; Dietrich, F.; Droeder, K. Current status and challenges for automotive battery production technologies. *Nat. Energy* **2018**, *3*, 290–300.

[8] Choi, J. W.; Aurbach, D. Promise and reality of post-lithium-ion batteries with high energy densities. *Nat. Rev. Mater.* **2016**, *1*, 16013.

[9] Zhang, E. H.; Hu, X.; Meng, L. Z.; Qiu, M.; Chen, J. X.; Liu, Y. J.; Liu, G. Y.; Zhuang, Z. C.; Zheng, X. B.; Zheng, L. R. et al. Single-atom yttrium engineering Janus electrode for rechargeable Na-S batteries. *J. Am. Chem. Soc.* **2022**, *144*, 18995–19007.

[10] Zhuang, Z. C.; Li, Y. H.; Yu, R. H.; Xia, L. X.; Yang, J. R.; Lang, Z. Q.; Zhu, J. X.; Huang, J. Z.; Wang, J. O.; Wang, Y. et al. Reversely trapping atoms from a perovskite surface for high-performance and durable fuel cell cathodes. *Nat. Catal.* **2022**, *5*, 300–310.

[11] Cheng, X. B.; Zhang, R.; Zhao, C. Z.; Zhang, Q. Toward safe lithium metal anode in rechargeable batteries: A review. *Chem. Rev.* **2017**, *117*, 10403–10473.

[12] Liu, J.; Bao, Z. N.; Cui, Y.; Dufek, E. J.; Goodenough, J. B.; Khalifah, P.; Li, Q. Y.; Liaw, B. Y.; Liu, P.; Manthiram, A. et al. Pathways for practical high-energy long-cycling lithium metal batteries. *Nat. Energy* **2019**, *4*, 180–186.

[13] Tikekar, M. D.; Choudhury, S.; Tu, Z. Y.; Archer, L. A. Design principles for electrolytes and interfaces for stable lithium-metal batteries. *Nat. Energy* **2016**, *1*, 16114.

[14] Zhang, X. Q.; Jin, Q.; Nan, Y. L.; Hou, L. P.; Li, B. Q.; Chen, X.; Jin, Z. H.; Zhang, X. T.; Huang, J. Q.; Zhang, Q. Electrolyte structure of lithium polysulfides with anti-reductive solvent shells for practical lithium-sulfur batteries. *Angew. Chem., Int. Ed.* **2021**, *60*, 15503–15509.

[15] Wang, R. H.; Cui, W. S.; Chu, F. L.; Wu, F. X. Lithium metal anodes: Present and future. *J. Energy Chem.* **2020**, *48*, 145–159.

[16] Zhao, M.; Li, X. Y.; Chen, X.; Li, B. Q.; Kaskel, S.; Zhang, Q.; Huang, J. Q. Promoting the sulfur redox kinetics by mixed organodiselenides in high-energy-density lithium-sulfur batteries. *eScience* **2021**, *1*, 44–52.

[17] Piao, Z. H.; Xiao, P. T.; Luo, R. P.; Ma, J. B.; Gao, R. H.; Li, C.; Tan, J. Y.; Yu, K.; Zhou, G. M.; Cheng, H. M. Constructing a stable interface layer by tailoring solvation chemistry in carbonate electrolytes for high-performance lithium-metal batteries. *Adv. Mater.* **2022**, *34*, 2108400.

[18] Kang, Q.; Li, Y.; Zhuang, Z. C.; Wang, D. S.; Zhi, C. Y.; Jiang, P. K.; Huang, X. Y. Dielectric polymer based electrolytes for high-performance all-solid-state lithium metal batteries. *J. Energy Chem.* **2022**, *69*, 194–204.

[19] Bruce, P. G.; Freunberger, S. A.; Hardwick, L. J.; Tarascon, J. M. Li-O_2 and Li-S batteries with high energy storage. *Nat. Mater.* **2012**, *11*, 19–29.

[20] Pang, Q.; Shyamsunder, A.; Narayanan, B.; Kwok, C. Y.; Curtiss, L. A.; Nazar, L. F. Tuning the electrolyte network structure to invoke quasi-solid state sulfur conversion and suppress lithium dendrite formation in Li-S batteries. *Nat. Energy* **2018**, *3*, 783–791.

[21] Service, R. F. Lithium-sulfur batteries poised for leap. *Science* **2018**, *359*, 1080–1081.

[22] Sun, C. B.; Sheng, J. Z.; Zhang, Q.; Gao, R. H.; Han, Z. Y.; Li, C.; Xiao, X.; Qiu, L.; Zhou, G. M. Self-extinguishing Janus separator with high safety for flexible lithium-sulfur batteries. *Sci. China Mater.* **2022**, *65*, 2169–2178.

[23] Chen, R. J.; Zhao, T.; Wu, F. From a historic review to horizons beyond: Lithium-sulphur batteries run on the wheels. *Chem. Commun.* **2015**, *51*, 18–33.

[24] Li, C.; Zhang, Q.; Sheng, J. Z.; Chen, B.; Gao, R. H.; Piao, Z. H.; Zhong, X. W.; Han, Z. Y.; Zhu, Y. F.; Wang, J. L. et al. A quasi-intercalation reaction for fast sulfur redox kinetics in solid-state lithium-sulfur batteries. *Energy Environ. Sci.* **2022**, *15*, 4289–4300.

[25] Li, X.; Guan, Q. H.; Zhuang, Z. C.; Zhang, Y. Z.; Lin, Y. H.; Wang, J.; Shen, C. Y.; Lin, H. Z.; Wang, Y. L.; Zhan, L. et al. Ordered mesoporous carbon grafted MXene catalytic heterostructure as Li-ion kinetic pump toward high-efficient sulfur/sulfide conversions for Li-S batteries. *ACS Nano* **2023**, *17*, 1653–1662.

[26] Wang, J.; Jia, L. J.; Liu, H. T.; Wang, C.; Zhong, J.; Xiao, Q. B.; Yang, J.; Duan, S. R.; Feng, K.; Liu, N. et al. Multi-ion modulated single-step synthesis of a nanocarbon embedded with a defect-rich nanoparticle catalyst for a high loading sulfur cathode. *ACS Appl. Mater. Interfaces* **2020**, *12*, 12727–12735.

[27] Wang, J.; Hu, H. M.; Duan, S. R.; Xiao, Q. B.; Zhang, J.; Liu, H. T.; Kang, Q.; Jia, L. J.; Yang, J.; Xu, W. L. et al. Construction of moisture-stable lithium diffusion-controlling layer toward high performance dendrite-free lithium anode. *Adv. Funct. Mater.* **2022**, *32*, 2110468.

[28] Ren, X. D.; Liu, Z. F.; Zhang, M.; Li, D. S.; Yuan, S. X.; Lu, C. X. Review of cathode in advanced Li-S batteries: The effect of doping atoms at micro levels. *ChemElectroChem.* **2021**, *8*, 3457–3471.

[29] Liu, W. L.; Fan, X. J.; Xu, B.; Chen, P.; Tang, D. J.; Meng, F. C.; Zhou, R. L.; Liu, J. H. MnO-inlaid hierarchically porous carbon hybrid for lithium-sulfur batteries. *Nano Select* **2021**, *2*, 573–580.

[30] Yu, S. L.; Sun, Y. J.; Song, L. X.; Cao, X.; Chen, L.; An, X. T.; Liu, X. H.; Cai, W. L.; Yao, T.; Song, Y. Z. et al. Vanadium atom modulated electrocatalyst for accelerated Li-S chemistry. *Nano Energy* **2021**, *89*, 106414.

[31] Gao, X. J.; Yang, X. F.; Li, M. S.; Sun, Q.; Liang, J. N.; Luo, J.; Wang, J. W.; Li, W. H.; Liang, J. W.; Liu, Y. L. et al. Cobalt-doped SnS_2 with dual active centers of synergistic absorption-catalysis effect for high-S loading Li-S batteries. *Adv. Funct. Mater.* **2019**, *29*, 1806724.

[32] Park, J.; Yu, B. C.; Park, J. S.; Choi, J. W.; Kim, C.; Sung, Y. E.; Goodenough, J. B. Tungsten disulfide catalysts supported on a carbon cloth interlayer for high performance Li-S battery. *Adv. Energy Mater.* **2017**, *7*, 1602567.

[33] Han, Z. Y.; Ren, H. R.; Huang, Z. J.; Zhang, Z. J.; Zhang, Y. B.; Gu, S. C.; Zhang, C.; Liu, W. H.; Yang, J. L.; Zhou, G. M.; Yang, Q. H. et al. A permselective coating protects lithium anode toward a practical lithium-sulfur battery. *ACS Nano* **2013**, *17*, 4453–4462.

[34] Zhao, Y. Y.; Ye, Y. S.; Wu, F.; Li, Y. J.; Li, L.; Chen, R. J. Anode interface engineering and architecture design for high-performance lithium-sulfur batteries. *Adv. Mater.* **2019**, *31*, 1806532.

[35] Lin, D. C.; Liu, Y.; Pei, A.; Cui, Y. Nanoscale perspective: Materials designs and understandings in lithium metal anodes. *Nano Res.* **2017**, *10*, 4003–4026.

[36] Chen, P.; Wang, T. Y.; Tang, F. L.; Chen, G. L.; Wang, C. Y. Elaborate interface design of CoS_2/Fe_7S_8/NG heterojunctions modified on a polypropylene separator for efficient lithium-sulfur batteries. *Chem. Eng. J.* **2022**, *446*, 136990.

[37] Sheng, J. Z.; Zhang, Q.; Sun, C. B.; Wang, J. X.; Zhong, X. W.; Chen, B.; Li, C.; Gao, R. H.; Han, Z. Y.; Zhou, G. M. Crosslinked nanofiber-reinforced solid-state electrolytes with polysulfide fixation effect towards high safety flexible lithium-sulfur batteries. *Adv. Funct. Mater.* **2022**, *32*, 2203272.

[38] Li, Y. J.; Wu, J. B.; Zhang, B.; Wang, W. Y.; Zhang, G. Q.; Seh, Z. W.; Zhang, N.; Sun, J.; Huang, L.; Jiang, J. J. et al. Fast conversion and controlled deposition of lithium (poly)sulfides in lithium-sulfur batteries using high-loading cobalt single atoms. *Energy Storage Mater.* **2020**, *30*, 250–259.

[39] Naguib, M.; Mashtalir, O.; Carle, J.; Presser, V.; Lu, J.; Hultman, L.; Gogotsi, Y.; Barsoum, M. W. Two-dimensional transition metal carbides. *ACS Nano* **2012**, *6*, 1322–1331.

[40] Naguib, M.; Mochalin, V. N.; Barsoum, M. W.; Gogotsi, Y. 25th Anniversary article: MXenes: A new family of two-dimensional materials. *Adv. Mater.* **2014**, *26*, 992–1005.

[41] Ronchi, R. M.; Arantes, J. T.; Santos, S. F. Synthesis, structure, properties and applications of MXenes: Current status and perspectives. *Ceram. Int.* **2019**, *45*, 18167–18188.

[42] Naguib, M.; Come, J.; Dyatkin, B.; Presser, V.; Taberna, P. L.; Simon, P.; Barsoum, M. W.; Gogotsi, Y. MXene: A promising transition metal carbide anode for lithium-ion batteries. *Electrochem. Commun.* **2012**, *16*, 61–64.

[43] Deysher, G.; Shuck, C. E.; Hantanasirisakul, K.; Frey, N. C.; Foucher, A. C.; Maleski, K.; Sarycheva, A.; Shenoy, V. B.; Stach, E. A.; Anasori, B. et al. Synthesis of Mo_4ValC_4 MAX Phase and two-dimensional Mo_4VC_4 MXene with five atomic layers of transition metals. *ACS Nano* **2020**, *14*, 204–217.

[44] Jin, Q.; Zhang, N.; Zhu, C. C.; Gao, H.; Zhang, X. T. Rationally designing S/$Ti_3C_2T_x$ as a cathode material with an interlayer for high-rate and long-cycle lithium-sulfur batteries. *Nanoscale* **2018**, *10*, 16935–16942.

[45] Li, T. F.; Yao, L. L.; Liu, Q. L.; Gu, J. J.; Luo, R. C.; Li, J. H.; Yan, X. D.; Wang, W. Q.; Liu, P.; Chen, B. et al. Fluorine-free synthesis of high-purity $Ti_3C_2T_x$ (T = OH, O) via alkali treatment. *Angew. Chem., Int. Ed.* **2018**, *57*, 6115–6119.

[46] Pang, S. Y.; Wong, Y. T.; Yuan, S. G.; Liu, Y.; Tsang, M. K.; Yang, Z. B.; Huang, H. T.; Wong, W. T.; Hao, J. H. Universal strategy for HF-free facile and rapid synthesis of two-dimensional MXenes as multifunctional energy materials. *J. Am. Chem. Soc.* **2019**, *141*, 9610–9616.

[47] Li, M.; Lu, J.; Luo, K.; Li, Y. B.; Chang, K. K.; Chen, K.; Zhou, J.; Rosen, J.; Hultman, L.; Eklund, P. et al. Element replacement approach by reaction with Lewis acidic molten salts to synthesize nanolaminated MAX phases and MXenes. *J. Am. Chem. Soc.* **2019**, *141*, 4730–4737.

[48] Jiang, J. Z.; Bai, S. S.; Zou, J.; Liu, S.; Hsu, J. P.; Li, N.; Zhu, G. Y.; Zhuang, Z. C.; Kang, Q.; Zhang, Y. Z. Improving stability of MXenes. *Nano Res.* **2022**, *15*, 6551–6567.

[49] Braff, W. A.; Mueller, J. M.; Trancik, J. E. Value of storage

technologies for wind and solar energy. *Nat. Clim. Change* **2016**, *6*, 964–969.

[50] Dong, Y. F.; Zheng, S. H.; Qin, J. Q.; Zhao, X. J.; Shi, H. D.; Wang, X. H.; Chen, J.; Wu, Z. S. All-MXene-based integrated electrode constructed by Ti_3C_2 nanoribbon framework host and nanosheet interlayer for high-energy-density Li-S batteries. *ACS Nano* **2018**, *12*, 2381–2388.

[51] Li, H.; Liu, A. M.; Ren, X. F.; Yang, Y. N.; Gao, L. G.; Fan, M. Q.; Ma, T. L. A black phosphorus/Ti_3C_2 MXene nanocomposite for sodium-ion batteries: A combined experimental and theoretical study. *Nanoscale* **2019**, *11*, 19862–19869.

[52] Guo, X.; Xie, X. Q.; Choi, S.; Zhao, Y. F.; Liu, H.; Wang, C. Y.; Chang, S.; Wang, G. X. Sb_2O_3/MXene ($Ti_3C_2T_x$) hybrid anode materials with enhanced performance for sodium-ion batteries. *J. Mater. Chem. A* **2017**, *5*, 12445–12452.

[53] Wu, J. B.; Li, Q.; Shuck, C. E.; Maleski, K.; Alshareef, H. N.; Zhou, J.; Gogotsi, Y.; Huang, L. An aqueous 2.1 V pseudocapacitor with MXene and V-MnO_2 electrodes. *Nano Res.* **2022**, *15*, 535–541.

[54] Zeraati, A. S.; Mirkhani, S. A.; Sun, P. C.; Naguib, M.; Braun, P. V.; Sundararaj, U. Improved synthesis of $Ti_3C_2T_x$ MXenes resulting in exceptional electrical conductivity, high synthesis yield, and enhanced capacitance. *Nanoscale* **2021**, *13*, 3572–3580.

[55] Jiang, X. T.; Kuklin, A. V.; Baev, A.; Ge, Y. Q.; Ågren, H.; Zhang, H.; Prasad, P. N. Two-dimensional MXenes: From morphological to optical, electric, and magnetic properties and applications. *Phys. Rep.* **2020**, *848*, 1–58.

[56] Lang, Z. Q.; Zhuang, Z. C.; Li, S. K.; Xia, L. X.; Zhao, Y.; Zhao, Y. L.; Han, C. H.; Zhou, L. MXene surface terminations enable strong metal–support interactions for efficient methanol oxidation on palladium. *ACS Appl. Mater. Interfaces* **2020**, *12*, 2400–2406.

[57] Li, Z. L.; Zhuang, Z. C.; Lv, F.; Zhu, H.; Zhou, L.; Luo, M. C.; Zhu, J. X.; Lang, Z. Q.; Feng, S. H.; Chen, W. et al. The marriage of the FeN_4 moiety and MXene boosts oxygen reduction catalysis: Fe 3d electron delocalization matters. *Adv. Mater.* **2018**, *30*, 1803220.

[58] Shang, M. W.; Shovon, O. G.; Wong, F. E. Y.; Niu, J. J. A BF_3-doped MXene dual-layer interphase for a reliable lithium-metal anode. *Adv. Mater.* **2023**, *35*, 2210111.

[59] Gu, J. N.; Chen, H.; Shi, Y.; Cao, Z. J.; Du, Z. G.; Li, B.; Yang, S. B. Eliminating lightning-rod effect of lithium anodes via sine-wave analogous MXene layers. *Adv. Energy Mater.* **2022**, *12*, 2201181.

[60] Zhang, D.; Wang, S.; Li, B.; Gong, Y. J.; Yang, S. B. Horizontal growth of lithium on parallelly aligned MXene layers towards dendrite-free metallic lithium anodes. *Adv. Mater.* **2019**, *31*, 1901820.

[61] Liang, X.; Garsuch, A.; Nazar, L. F. Sulfur cathodes based on conductive MXene nanosheets for high-performance lithium-sulfur batteries. *Angew. Chem., Int. Ed.* **2015**, *54*, 3907–3911.

[62] Rao, D. W.; Zhang, L. Y.; Meng, Z. S.; Zhang, X. R.; Wang, Y. H.; Qiao, G. J.; Shen, X. Q.; Xia, H.; Liu, J. H.; Lu, R. F. Ultrahigh energy storage and ultrafast ion diffusion in borophene-based anodes for rechargeable metal ion batteries. *J. Mater. Chem. A* **2017**, *5*, 2328–2338.

[63] Liang, X.; Rangom, Y.; Kwok, C. Y.; Pang, Q.; Nazar, L. F. Interwoven MXene nanosheet/carbon-nanotube composites as Li-S cathode hosts. *Adv. Mater.* **2017**, *29*, 1603040.

[64] Wang, D. S.; Li, F.; Lian, R. Q.; Xu, J.; Kan, D. X.; Liu, Y. H.; Chen, G.; Gogotsi, Y.; Wei, Y. J. A general atomic surface modification strategy for improving anchoring and electrocatalysis behavior of $Ti_3C_2T_2$ MXene in lithium-sulfur batteries. *ACS Nano* **2019**, *13*, 11078–11086.

[65] Chen, Li.; Yue, L. G.; Wang, X. Y.; Wu, S. Y.; Wang, W.; Lu, D. Z.; Liu, X.; Zhou, W. L.; Li, Y. Y. Synergistically accelerating adsorption–electrocataysis of sulfur species via interfacial built-in electric field of SnS_2-MXene Mott-Schottky heterojunction in Li-S batteries. *Small* **2023**, *19*, 2206462.

[66] Huang, S. Z.; Wang, Z. H.; Von Lim, Y.; Wang, Y.; Li, Y.; Zhang, D. H.; Yang, H. Y. Recent advances in heterostructure engineering for lithium-sulfur batteries. *Adv. Energy Mater.* **2021**, *11*, 2003689.

[67] Pang, J. B.; Chang, B.; Liu, H.; Zhou, W. J. Potential of MXene-based heterostructures for energy conversion and storage. *ACS Energy Lett.* **2022**, *7*, 78–96.

[68] Alferov, Z. I. The history and future of semiconductor heterostructures. *Semiconductors* **1998**, *32*, 1–14.

[69] Huang, J. Z.; Zhuang, Z. C.; Zhao, Y.; Chen, J. Q.; Zhuo, Z. W.; Liu, Y. W.; Lu, N.; Li, H. Q.; Zhai, T. Y. Back-gated van der Waals heterojunction manipulates local charges toward fine-tuning hydrogen evolution. *Angew. Chem., Int. Ed.* **2022**, *61*, e202203522.

[70] Zhuang, Z. C.; Xia, L. X.; Huang, J. Z.; Zhu, P.; Li, Y.; Ye, C. L.; Xia, M. G.; Yu, R. H.; Lang, Z. Q.; Zhu, J. X. et al. Continuous modulation of electrocatalytic oxygen reduction activities of single-atom catalysts through p-n junction rectification. *Angew. Chem., Int. Ed.* **2022**, *62*, e202212335.

[71] Zhang, B.; Luo, C.; Zhou, G. M.; Pan, Z. Z.; Ma, J. B.; Nishihara, H.; He, Y. B.; Kang, F. Y.; Lv, W.; Yang, Q. H. Lamellar MXene composite aerogels with sandwiched carbon nanotubes enable stable lithium-sulfur batteries with a high sulfur loading. *Adv. Funct. Mater.* **2021**, *31*, 2100793.

[72] Gan, R. Y.; Yang, N.; Dong, Q.; Fu, N.; Wu, R.; Li, C. P.; Liao, Q.; Li, J.; Wei, Z. D. Enveloping ultrathin Ti_3C_2 nanosheets on carbon fibers: A high-density sulfur loaded lithium-sulfur battery cathode with remarkable cycling stability. *J. Mater. Chem. A* **2020**, *8*, 7253–7260.

[73] Tang, X. Y.; Gan, R. Y.; Tan, L. Q.; Tong, C.; Li, C. P.; Wei, Z. D. 3D Net-like GO-d-$Ti_3C_2T_x$ MXene aerogels with catalysis/adsorption dual effects for high-performance lithium-sulfur batteries. *ACS Appl. Mater. Interfaces* **2021**, *13*, 55235–55242.

[74] Liu, P.; Qu, L.; Tian, X. L.; Yi, Y. K.; Xia, J. X.; Wang, T.; Nan, J. Z.; Yang, P.; Wang, T.; Fang, B. R. et al. $Ti_3C_2T_x$/graphene oxide free-standing membranes as modified separators for lithium-sulfur batteries with enhanced rate performance. *ACS Appl. Energy Mater.* **2020**, *3*, 2708–2718.

[75] Zhou, H. Y.; Sui, Z. Y.; Amin, K.; Lin, L. W.; Wang, H. Y.; Han, B. H. Investigating the electrocatalysis of a Ti_3C_2/carbon hybrid in polysulfide conversion of lithium-sulfur batteries. *ACS Appl. Mater. Interfaces* **2020**, *12*, 13904–13913.

[76] Zhang, H.; Yang, L.; Zhang, P. G.; Lu, C. J.; Sha, D. W.; Yan, B. Z.; He, W.; Zhou, M.; Zhang, W.; Pan, L. et al. MXene-derived Ti_nO_{2n-1} quantum dots distributed on porous carbon nanosheets for stable and long-life Li-S batteries: Enhanced polysulfide mediation via defect engineering. *Adv. Mater.* **2021**, *33*, 2008447.

[77] Zhao, J.; Qi, Y. R.; Yang, Q. J.; Huang, T.; Wang, H.; Wang, Y. Y.; Niu, Y. B.; Liu, Y. J.; Bao, S. J.; Xu, M. W. Chessboard structured electrode design for Li-S batteries based on MXene nanosheets. *Chem. Eng. J.* **2022**, *429*, 131997.

[78] Bao, W. Z.; Xie, X. Q.; Xu, J.; Guo, X.; Song, J. J.; Wu, W. J.; Su, D. W.; Wang, G. X. Confined sulfur in 3D MXene/reduced graphene oxide hybrid nanosheets for lithium-sulfur battery. *Chem.—Eur. J.* **2017**, *23*, 12613–12619.

[79] Xia, J.; Chen, W. X.; Yang, Y.; Guan, X. G.; Yang, T.; Xiao, M. J.; Zhang, S. C.; Xing, Y. L.; Lu, X.; Zhuo, G. M. *In-situ* growth of ultrathin sulfur microcrystal on MXene-based 3D matrice for flexible lithium-sulfur batteries. *EcoMat.* **2022**, *4*, e12183.

[80] Wang, T.; Liu, Y. Y.; Zhang, X. M.; Wang, J. Y.; Zhang, Y. G.; Li, Y. B.; Zhu, Y. J.; Li, G. R.; Wang, X. Interspersing partially oxidized V_2C nanosheets and carbon nanotubes toward multifunctional polysulfide barriers for high-performance lithium-sulfur batteries. *ACS Appl. Mater. Interfaces* **2021**, *13*, 56085–56094.

[81] Jiao, L.; Zhang, C.; Geng, C. N.; Wu, S. C.; Li, H.; Lv, W.; Tao, Y.; Chen, Z. J.; Zhou, G. M.; Li, J. et al. Capture and catalytic conversion of polysulfides by *in situ* built TiO_2-MXene heterostructures for lithium-sulfur batteries. *Adv. Energy Mater.* **2019**, *9*, 1900219.

[82] Wei, C. H.; Tian, M.; Wang, M. L.; Shi, Z. X.; Yu, L. H.; Li, S.; Fan, Z. D.; Yang, R. Z.; Sun, J. Y. Universal *in situ* crafted MO_x-MXene heterostructures as heavy and multifunctional hosts for 3D-printed Li-S batteries. *ACS Nano* **2020**, *14*, 16073–16084.

[83] Wang, Z. G.; Yu, K.; Feng, Y.; Qi, R. J.; Ren, J.; Zhu, Z. Q. VO_2(p)-V_2C(MXene) grid structure as a lithium polysulfide catalytic host

for high-performance Li-S battery. *ACS Appl. Mater. Interfaces* **2019**, *11*, 44282–44292.
[84] Xu, M. Y.; Wu, T. L.; Qi, J.; Zhou, D.; Xiao, Z. B. V_2C/VO_2 nanoribbon intertwined nanosheet dual heterostructure for highly flexible and robust lithium-sulfur batteries. *J. Mater. Chem. A* **2021**, *9*, 21429–21439.
[85] Wu, S. Y.; Wang, W.; Shan, J. W.; Wang, X. Y.; Lu, D. Z.; Zhu, J. L.; Liu, Z. G.; Yue, L. G.; Li, Y. Y. Conductive 1T-VS_2-MXene heterostructured bidirectional electrocatalyst enabling compact Li-S batteries with high volumetric and areal capacity. *Energy Storage Mater.* **2022**, *49*, 153–163.
[86] Tian, S. H.; Zeng, Q.; Liu, G.; Huang, J. J.; Sun, X.; Wang, D.; Yang, H. C.; Liu, Z.; Mo, X. C.; Wang, Z. X. et al. Multi-dimensional composite frame as bifunctional catalytic medium for ultra-fast charging lithium-sulfur battery. *Nano-Micro Lett.* **2022**, *14*, 196.
[87] Yang, C. Y.; Li, Y.; Peng, W. C.; Zhang, F. B.; Fan, X. B. *In situ* N-doped CoS_2 anchored on MXene toward an efficient bifunctional catalyst for enhanced lithium-sulfur batteries. *Chem. Eng. J.* **2022**, *427*, 131792.
[88] Wang, W.; Huai, L. Y.; Wu, S. Y.; Shan, J. W.; Zhu, J. L.; Liu, Z. G.; Yue, L. G.; Li, Y. Y. Ultrahigh-volumetric-energy-density lithium-sulfur batteries with lean electrolyte enabled by cobalt-doped $MoSe_2/Ti_3C_2T_x$ MXene bifunctional catalyst. *ACS Nano* **2021**, *15*, 11619–11633.
[89] Ye, Z. Q.; Jiang, Y.; Li, L.; Wu, F.; Chen, R. J. Enhanced catalytic conversion of polysulfide using 1D CoTe and 2D MXene for heat-resistant and lean-electrolyte Li-S batteries. *Chem. Eng. J.* **2022**, *430*, 132734.
[90] Wang, H.; Cui, Z.; He, S. A.; Zhu, J. Q.; Luo, W.; Liu, Q.; Zou, R. J. Construction of ultrathin layered MXene-TiN heterostructure enabling favorable catalytic ability for high-areal-capacity lithium-sulfur batteries. *Nano-Micro Lett.* **2022**, *14*, 189.
[91] Meng, R. J.; Deng, Q. Y.; Peng, C. X.; Chen, B. J.; Liao, K. X.; Li, L. J.; Yang, Z. Y.; Yang, D. L.; Zheng, L.; Zhang, C. et al. Two-dimensional organic-inorganic heterostructures of *in situ*-grown layered COF on Ti_3C_2 MXene nanosheets for lithium-sulfur batteries. *Nano Today* **2020**, *35*, 100991.
[92] Li, P. Y.; Lv, H. W.; Li, Z. L.; Meng, X. P.; Lin, Z.; Wang, R. H.; Li, X. J. The electrostatic attraction and catalytic effect enabled by ionic-covalent organic nanosheets on MXene for separator modification of lithium-sulfur batteries. *Adv. Mater.* **2021**, *33*, 2007803.
[93] Wen, C. Y.; Guo, D. H.; Zheng, X. Z.; Li, H. F.; Sun, G. B. Hierarchical *n*MOF-867/MXene nanocomposite for chemical adsorption of polysulfides in lithium-sulfur batteries. *ACS Appl. Energy Mater.* **2021**, *4*, 8231–8241.
[94] Jiang, G. Y.; Zheng, N.; Chen, X.; Ding, G. Y.; Li, Y. H.; Sun, F. G.; Li, Y. S. In-situ decoration of MOF-derived carbon on nitrogen-doped ultrathin MXene nanosheets to multifunctionalize separators for stable Li-S batteries. *Chem. Eng. J.* **2019**, *373*, 1309–1318.
[95] Wang, J. T.; Zhao, T. K.; Yang, Z. H.; Chen, Y.; Liu, Y.; Wang, J. X.; Zhai, P. F.; Wu, W. J. MXene-based Co, N-codoped porous carbon nanosheets regulating polysulfides for high-performance lithium-sulfur batteries. *ACS Appl. Mater. Interfaces* **2019**, *11*, 38654–38662.
[96] Zong, H.; Hu, L.; Wang, Z. G.; Qi, R. J.; Yu, K.; Zhu, Z. Q. Metal-organic frameworks-derived CoP anchored on MXene toward an efficient bifunctional electrode with enhanced lithium storage. *Chem. Eng. J.* **2021**, *416*, 129102.
[97] Ye, Z. Q.; Jiang, Y.; Li, L.; Wu, F.; Chen, R. J. Self-assembly of 0D-2D heterostructure electrocatalyst from MOF and MXene for boosted lithium polysulfide conversion reaction. *Adv. Mater.* **2021**, *33*, 2101204.
[98] Zhang, Y. Q.; Tang, W. W.; Zhan, R. M.; Liu, H.; Chen, H.; Yang, J. G.; Xu, M. W. An N-doped porous carbon/MXene composite as a sulfur host for lithium-sulfur batteries. *Inorg. Chem. Front.* **2019**, *6*, 2894–2899.
[99] Wang, J. T.; Zhai, P. F.; Zhao, T. K.; Li, M. J.; Yang, Z. H.; Zhang, H. Q.; Huang, J. J. Laminar MXene-Nafion-modified separator with highly inhibited shuttle effect for long-life lithium-sulfur batteries. *Electrochim. Acta* **2019**, *320*, 134558.
[100] Cao, Y. W.; Jia, Y. C.; Meng, X. D.; Fan, X. Y.; Zhang, J.; Zhou, J.; Matoga, D.; Bielawski, C. W.; Geng, J. X. Covalently grafting conjugated porous polymers to MXene offers a two-dimensional sandwich-structured electrocatalytic sulfur host for lithium-sulfur batteries. *Chem. Eng. J.* **2022**, *446*, 137365.
[101] Zhang, D.; Wang, S.; Hu, R. M.; Gu, J. N.; Cui, Y. L. S.; Li, B.; Chen, W. H.; Liu, C. T.; Shang, J. X.; Yang, S. B. Catalytic conversion of polysulfides on single atom zinc implanted MXene toward high-rate lithium-sulfur batteries. *Adv. Funct. Mater.* **2020**, *30*, 2002471.
[102] Du, Z. G.; Wu, C.; Chen, Y. C.; Zhu, Q.; Cui, Y. L. S.; Wang, H. Y.; Zhang, Y. Z.; Chen, X.; Shang, J. X.; Li, B. et al. High-entropy carbonitride MAX phases and their derivative MXenes. *Adv. Energy Mater.* **2022**, *12*, 2103228.
[103] Guo, X.; Zhang, H.; Yao, Y. Y.; Xiao, C. M.; Yan, X.; Chen, K.; Qi, J. W.; Zhou, Y. J.; Zhu, Z. G.; Sun, X. Y. et al. Derivatives of two-dimensional MXene-MOFs heterostructure for boosting peroxymonosulfate activation: Enhanced performance and synergistic mechanism. *Appl. Catal. B: Environ.* **2023**, *323*, 122136.
[104] Yang, X.; Wang, Q.; Zhu, K.; Ye, K.; Wang, G. L.; Cao, D. X.; Yan, J. 3D porous oxidation-resistant MXene/graphene architectures induced by *in situ* zinc template toward high-performance supercapacitors. *Adv. Funct. Mater.* **2021**, *31*, 2101087.
[105] Xiao, Z. B.; Li, Z. L.; Meng, X. P.; Wang, R. H. MXene-engineered lithium-sulfur batteries. *J. Mater. Chem. A* **2019**, *7*, 22730–22743.
[106] Qu, Y. H.; Zhang, Z. A.; Zhang, X. H.; Ren, G. D.; Lai, Y. Q.; Liu, Y. X.; Li, J. Highly ordered nitrogen-rich mesoporous carbon derived from biomass waste for high-performance lithium-sulfur batteries. *Carbon* **2015**, *84*, 399–408.
[107] Jayaprakash, N.; Shen, J.; Moganty, S. S.; Corona, A.; Archer, L. A. Porous hollow carbon@sulfur composites for high-power lithium-sulfur batteries. *Angew. Chem., Int. Ed.* **2011**, *50*, 5904–5908.
[108] Gueon, D.; Hwang, J. T.; Yang, S. B.; Cho, E.; Sohn, K.; Yang, D. K.; Moon, J. H. Spherical icroporous carbon nanotube particles with ultrahigh sulfur loading for lithium-sulfur battery cathodes. *ACS Nano* **2018**, *12*, 226–233.
[109] Li, X.; Cheng, X. B.; Gao, M. X.; Ren, D. W.; Liu, Y. F.; Guo, Z. X.; Shang, C. X.; Sun, L. X.; Pan, H. G. Amylose-derived macrohollow core and microporous shell carbon spheres as sulfur host for superior lithium-sulfur battery cathodes. *ACS Appl. Mater. Interfaces* **2017**, *9*, 10717–10729.
[110] Zhang, Y. Z.; Wang, R. C.; Tang, W. Q.; Zhan, L.; Zhao, S. L.; Kang, Q.; Wang, Y. L.; Yang, S. B. Efficient polysulfide barrier of a graphene aerogel-carbon nanofibers-Ni network for high-energy-density lithium-sulfur batteries with ultrahigh sulfur content. *J. Mater. Chem. A* **2018**, *6*, 20926–20938.
[111] Zhang, Y. Z.; Xu, G. X.; Kang, Q.; Zhan, L.; Tang, W. Q.; Yu, Y. X.; Shen, K. L.; Wang, H. C.; Chu, X.; Wang, J. Y. et al. Synergistic electrocatalysis of polysulfides by a nanostructured VS_4-carbon nanofiber functional separator for high-performance lithium-sulfur batteries. *J. Mater. Chem. A* **2019**, *7*, 16812–16820.
[112] Zhang, J.; Jia, L. J.; Lin, H. Z.; Wang, J. Advances and prospects of 2D graphene-based materials/hybrids for lithium metal-sulfur full battery: From intrinsic property to catalysis modification. *Adv. Energy Sustainability Res.* **2022**, *3*, 2100187.
[113] Zhu, J. X.; Tang, C. J.; Zhuang, Z. C.; Shi, C. W.; Li, N. R.; Zhou, L.; Mai, L. Q. Porous and low-crystalline manganese silicate hollow spheres wired by graphene oxide for high-performance lithium and sodium storage. *ACS Appl. Mater. Interfaces* **2017**, *9*, 24584–24590.
[114] Liang, X.; Hart, C.; Pang, Q.; Garsuch, A.; Weiss, T.; Nazar, L. F. A highly efficient polysulfide mediator for lithium-sulfur batteries. *Nat. Commun.* **2015**, *6*, 5682.
[115] Deville, S. Freeze-casting of porous ceramics: A review of current achievements and issues. *Adv. Eng. Mater.* **2008**, *10*, 155–169.
[116] Tang, H.; Li, W. L.; Pan, L. M.; Cullen, C. P.; Liu, Y.; Pakdel, A.; Long, D. H.; Yang, J.; Mcevoy, N.; Duesberg, G. S. et al. *In situ* formed protective barrier enabled by sulfur@titanium carbide

(MXene) ink for achieving high-capacity, long lifetime Li-S batteries. *Adv. Sci.* **2018**, *5*, 1800502.
[117] Pang, Q.; Liang, X.; Kwok, C. Y.; Nazar, L. F. Advances in lithium-sulfur batteries based on multifunctional cathodes and electrolytes. *Nat. Energy* **2016**, *1*, 16132.
[118] Liu, T. F.; Hu, H. L.; Ding, X. F.; Yuan, H. D.; Jin, C. B.; Nai, J. W.; Liu, Y. J.; Wang, Y.; Wan, Y. H.; Tao, X. Y. 12 years roadmap of the sulfur cathode for lithium sulfur batteries (2009–2020). *Energy Storage Mater.* **2020**, *30*, 346–366.
[119] Song, Y. Z.; Zhao, W.; Kong, L.; Zhang, L.; Zhu, X. Y.; Shao, Y. L.; Ding, F.; Zhang, Q.; Sun, J. Y.; Liu, Z. F. Synchronous immobilization and conversion of polysulfides on a VO_2-VN binary host targeting high sulfur load Li-S batteries. *Energy Environ. Sci.* **2018**, *11*, 2620–2630.
[120] Wu, C. Z.; Feng, F.; Xie, Y. Design of vanadium oxide structures with controllable electrical properties for energy applications. *Chem. Soc. Rev.* **2013**, *42*, 5157–5183.
[121] Qazilbash, M. M.; Brehm, M.; Chae, B. G.; Ho, P. C.; Andreev, G. Q.; Kim, B. J.; Yun, S. J.; Balatsky, A. V.; Maple, M. B.; Keilmann, F. et al. Mott transition in VO_2 revealed by infrared spectroscopy and nano-imaging. *Science* **2007**, *318*, 1750–1753.
[122] Qu, Y. J.; Shao, M. M.; Shao, Y. F.; Yang, M. Y.; Xu, J. C.; Kwok, C. T.; Shi, X. Q.; Lu, Z. G.; Pan, H. Ultra-high electrocatalytic activity of VS_2 nanoflowers for efficient hydrogen evolution reaction. *J. Mater. Chem. A* **2017**, *5*, 15080–15086.
[123] Ma, X. F.; Yin, L.; Zou, J. J.; Mi, W. B.; Wang, X. C. Strain-tailored valley polarization and magnetic anisotropy in two-dimensional 2H-VS_2/Cr_2C heterostructures. *J. Phys. Chem. C.* **2019**, *123*, 17440–17448.
[124] Salavati, M.; Rabczuk, T. Application of highly stretchable and conductive two-dimensional 1T VS_2 and Vse_2 as anode materials for Li-, Na- and Ca-ion storage. *Comput. Mater. Sci.* **2019**, *160*, 360–367.
[125] Li, M. Y.; Yang, D. W.; Biendicho, J. J.; Han, X.; Zhang, C. Q.; Liu, K.; Diao, J. F.; Li, J. S.; Wang, J.; Heggen, M. et al. Enhanced polysulfide conversion with highly conductive and electrocatalytic iodine-doped bismuth selenide nanosheets in lithium-sulfur batteries. *Adv. Funct. Mater.* **2022**, *32*, 2200529.
[126] Zhang, C. Q.; Biendicho, J. J.; Zhang, T.; Du, R. F.; Li, J. S.; Yang, X. H.; Arbiol, J.; Zhou, Y. T.; Morante, J. R.; Cabot, A. Combined high catalytic activity and efficient polar tubular nanostructure in urchin-like metallic $NiCo_2Se_4$ for high-performance lithium-sulfur batteries. *Adv. Funct. Mater.* **2019**, *29*, 1903842.
[127] Wang, J. L.; Du, R.; Yu, C. B.; Xu, C. Y.; Shi, Z. Y. Application of transition metal compounds in cathode materials for lithium-sulfur battery. *Ionics* **2022**, *28*, 5275–5288.
[128] Chen, Q.; Gong, Y. J. Applications and challenges of 2D materials in lithium metal batteries. *Mater. Lab* **2022**, *1*, 220034.
[129] Wang, M. X.; Fan, L. S.; Sun, X.; Guan, B.; Jiang, B.; Wu, X.; Tian, D.; Sun, K. N.; Qiu, Y.; Yin, X. J. et al. Nitrogen-doped $CoSe_2$ as a bifunctional catalyst for high areal capacity and lean electrolyte of Li-S battery. *ACS Energy Lett.* **2020**, *5*, 3041–3050.
[130] Ganesan, V.; Nam, K. H.; Park, C. M. Robust polyhedral $CoTe_2$-C nanocomposites as high-performance Li- and Na-Ion battery anodes. *ACS Appl. Energy Mater.* **2020**, *3*, 4877–4887.
[131] Chen, Z. L.; Chen, M.; Yan, X. X.; Jia, H. X.; Fei, B.; Ha, Y.; Qing, H. L.; Yang, H. Y.; Liu, M.; Wu, R. B. Vacancy occupation-driven polymorphic transformation in cobalt ditelluride for boosted oxygen evolution reaction. *ACS Nano* **2020**, *14*, 6968–6979.
[132] Wang, H. X.; Wang, Y. W.; Tan, L. X.; Fang, L.; Yang, X. H.; Huang, Z. Y.; Li, J.; Zhang, H. J.; Wang, Y. Component-controllable cobalt telluride nanoparticles encapsulated in nitrogen-doped carbon frameworks for efficient hydrogen evolution in alkaline conditions. *Appl. Catal. B: Environ.* **2019**, *244*, 568–575.
[133] Liang, Y.; Xia, T.; Chang, Z. S.; Xie, W. Y.; Li, Y. P.; Li, C. K.; Fan, R. M.; Wang, W. X.; Sui, Z. Y.; Chen, Q. Boric acid functionalized triazine-based covalent organic frameworks with dual-function for selective adsorption and lithium-sulfur battery cathode. *Chem. Eng. J.* **2022**, *437*, 135314.
[134] Hu, B.; Xu, J.; Fan, Z. J.; Xu, C.; Han, S. C.; Zhang, J. X.; Ma, L. B.; Ding, B.; Zhuang, Z. C.; Kang, Q. et al. Covalent organic framework based lithium-sulfur batteries: Materials, interfaces, and solid-state electrolytes. *Adv. Energy Mater.* **2023**, *13*, 2203540.
[135] Yang, Z. Y.; Peng, C. X.; Meng, R. J.; Zu, L. H.; Feng, Y. T.; Chen, B. J.; Mi, Y. L.; Zhang, C.; Yang, J. H. Hybrid anatase/rutile nanodots-embedded covalent organic frameworks with complementary polysulfide adsorption for high-performance lithium-sulfur batteries. *ACS Cent. Sci.* **2019**, *5*, 1876–1883.
[136] Zhang, X. H.; Dong, P. P.; Song, M. K. Metal-organic frameworks for high-energy lithium batteries with enhanced safety: Recent progress and future perspectives. *Batteries Supercaps* **2019**, *2*, 591–626.
[137] Hong, X. J.; Tang, X. Y.; Wei, Q.; Song, C. L.; Wang, S. Y.; Dong, R. F.; Cai, Y. P.; Si, L. P. Efficient encapsulation of small S_{2-4} molecules in MOF-derived flowerlike nitrogen-doped microporous carbon nanosheets for high-performance Li-S batteries. *ACS Appl. Mater. Interfaces* **2018**, *10*, 9435–9443.
[138] He, Y. B.; Chang, Z.; Wu, S. C.; Qiao, Y.; Bai, S. Y.; Jiang, K. Z.; He, P.; Zhou, H. S. Simultaneously inhibiting lithium dendrites growth and polysulfides shuttle by a flexible MOF-based membrane in Li-S batteries. *Adv. Energy Mater.* **2018**, *8*, 1802130.
[139] Xu, J.; Zhang, H.; Yu, F. T.; Cao, Y. J.; Liao, M. C.; Dong, X. L.; Wang, Y. G. Realizing all-climate Li-S batteries by using a porous sub-nano aromatic framework. *Angew. Chem., Int. Ed.* **2022**, *61*, e202211933.
[140] Cui, Y. L. S.; Cao, Z. J.; Zhang, Y. Z.; Chen, H.; Gu, J. N.; Du, Z. G.; Shi, Y. Z.; Li, B.; Yang, S. B. Single-atom sites on MXenes for energy conversion and storage. *Small Sci.* **2021**, *1*, 2100017.
[141] Han, Z. Y.; Zhao, S. Y.; Xiao, J. W.; Zhong, X. W.; Sheng, J. Z.; Lv, W.; Zhang, Q. F.; Zhou, G. M.; Cheng, H. M. Engineering *d-p* orbital hybridization in single-atom metal-embedded three-dimensional electrodes for Li-S Batteries. *Adv. Mater.* **2021**, *33*, 2105947.
[142] Zhang, S. L.; Ao, X.; Huang, J.; Wei, B.; Zhai, Y. L.; Zhai, D.; Deng, W. Q.; Su, C. L.; Wang, D. S.; Li, Y. D. Isolated single-atom Ni-N_5 catalytic site in hollow porous carbon capsules for efficient lithium-sulfur batteries. *Nano Lett.* **2021**, *21*, 9691–9698.
[143] Jin, C. Y.; Fan, S. J.; Zhuang, Z. C.; Zhou, Y. S. Single-atom nanozymes: From bench to bedside. *Nano Res.* **2023**, *16*, 1992–2002.
[144] Zhuang, Z. C.; Kang, Q.; Wang, D. S.; Li, Y. D. Single-atom catalysis enables long-life, high-energy lithium-sulfur batteries. *Nano Res.* **2020**, *13*, 1856–1866.
[145] Li, H.; Yu, B.; Zhuang, Z. C.; Sun, W. P.; Jia, B. H.; Ma, T. Y. A small change in the local atomic environment for a big improvement in single-atom catalysis. *J. Mater. Chem. A* **2021**, *9*, 4184–4192.
[146] Wei, C. L.; Tao, Y.; An, Y. L.; Tian, Y.; Zhang, Y. C.; Feng, J. K.; Qian, Y. T. Recent advances of emerging 2D MXene for stable and dendrite-free metal anodes. *Adv. Funct. Mater.* **2020**, *30*, 2004613.
[147] Xu, W.; Wang, J. L.; Ding, F.; Chen, X. L.; Nasybulin, E.; Zhang, Y. H.; Zhang, J. G. Lithium metal anodes for rechargeable batteries. *Energy Environ. Sci.* **2014**, *7*, 513–537.
[148] Tao, T.; Lu, S. G.; Fan, Y.; Lei, W. W.; Huang, S. M.; Chen, Y. Anode improvement in rechargeable lithium-sulfur batteries. *Adv. Mater.* **2017**, *29*, 1700542.
[149] Lu, W.; Wang, Zhao.; Sun, G. R.; Zhang, S. M.; Cong, L. N.; Lin, L.; Chen, S. R.; Liu, J.; Xie, H. M.; Liu, Y. L. Anchoring polysulfide with artificial solid electrolyte interphase for dendrite-free and low N/P ratio Li-S batteries. *J. Energy Chem.* **2023**, *80*, 32–39.
[150] Cao, Z. J.; Zhang, Y. Z.; Cui, Y. L. S.; Li, B.; Yang, S. B. Harnessing the unique features of MXenes for sulfur cathodes. *Tungsten* **2020**, *2*, 162–175.
[151] Shen, K.; Cao, Z. J.; Shi, Y. Z.; Zhang, Y. Z.; Li, B.; Yang, S. B. 3D printing lithium salt towards dendrite-free lithium anodes. *Energy Storage Mater.* **2021**, *35*, 108–113.
[152] Zhang, X. Y.; Lv, R. J.; Wang, A. X.; Guo, W. Q.; Liu, X. J.; Luo, J. Y. MXene aerogel scaffolds for high-rate lithium metal anodes. *Angew. Chem., Int. Ed.* **2018**, *57*, 15028–15033.
[153] Wang, C. Y.; Zheng, Z. J.; Feng, Y. Q.; Ye, H.; Cao, F. F.; Guo, Z. P. Topological design of ultrastrong MXene paper hosted Li

enables ultrathin and fully flexible lithium metal batteries. *Nano Energy* **2020**, *74*, 104817.

[154] Li, B.; Zhang, D.; Liu, Y.; Yu, Y. X.; Li, S. M.; Yang, S. B. Flexible Ti_3C_2 MXene-lithium film with lamellar structure for ultrastable metallic lithium anodes. *Nano Energy* **2017**, *39*, 654–661.

[155] Kang, Q.; Zhuang, Z. C.; Li, Yong.; Zuo, Y. Z.; Wang, J.; Liu, Y. J.; Shi, C. Q.; Chen, J.; Li, H. F.; Jiang, P. K. et al. Manipulating dielectric property of polymer coatings toward high-retention-rate lithium metal full batteries under harsh critical conditions. *Nano Res*., in press, https://doi.org/10.1007/s12274-023-5478-4.

[156] Cao, Z. J.; Zhu, Q.; Wang, S.; Zhang, D.; Chen, H.; Du, Z. G.; Li, B.; Yang, S. B. Perpendicular MXene arrays with periodic interspaces toward dendrite-free lithium metal anodes with high-rate capabilities. *Adv. Funct. Mater.* **2020**, *30*, 1908075.

[157] Shi, H. D.; Zhang, C. J.; Lu, P. F.; Dong, Y. F.; Wen, P. C.; Wu, Z. S. Conducting and lithiophilic MXene/graphene framework for high-capacity, dendrite-free lithium-metal anodes. *ACS Nano* **2019**, *13*, 14308–14318.

[158] Li, W. T.; Zhang, Y. F.; Li, H.; Chen, Z. J.; Shang, T. X.; Wu, Z. T.; Zhang, C.; Li, J.; Lv, W.; Tao, Y. et al. Layered MXene protected lithium metal anode as an efficient polysulfide blocker for lithium-sulfur batteries. *Batteries Supercaps* **2020**, *3*, 892–899.

[159] Zhao, F. F.; Zhai, P. B.; Wei, Y.; Yang, Z. L.; Chen, Q.; Zuo, J. H.; Gu, X. K.; Gong, Y. J. Constructing artificial SEI layer on lithiophilic MXene surface for high-performance lithium metal anodes. *Adv. Sci.* **2022**, *9*, 2103930.

[160] Guo, D.; Ming, F. W.; Shinde, D. B.; Cao, L.; Huang, G.; Li, C. Y.; Li, Z.; Yuan, Y. Y.; Hedhili, M. N.; Alshareef, H. N. et al. Covalent assembly of two-dimensional COF-on-MXene heterostructures enables fast charging lithium hosts. *Adv. Funct. Mater.* **2021**, *31*, 2101194.

[161] Wei, C. L.; Wang, Y. S.; Zhang, Y. C.; Tan, L. W.; Qian, Y.; Tao, Y.; Xiong, S. L.; Feng, J. K. Flexible and stable 3D lithium metal anodes based on self-standing MXene/COF frameworks for high-performance lithium-sulfur batteries. *Nano Res.* **2021**, *14*, 3576–3584.

[162] Yang, T. Z.; Qian, T.; Shen, X. W.; Wang, M. F.; Liu, S. S.; Zhong, J.; Yan, C. L.; Rosei, F. Single-cluster Au as an usher for deeply cyclable Li metal anodes. *J. Mater. Chem. A* **2019**, *7*, 14496–14503.

[163] Yang, C. P.; Yao, Y. G.; He, S. M.; Xie, H.; Hitz, E.; Hu, L. B. Ultrafine silver nanoparticles for seeded lithium deposition toward stable lithium metal anode. *Adv. Mater.* **2017**, *29*, 1702714.

[164] Yan, K.; Lu, Z. D.; Lee, H. W.; Xiong, F.; Hsu, P. C.; Li, Y. Z.; Zhao, J.; Chu, S.; Cui, Y. Selective deposition and stable encapsulation of lithium through heterogeneous seeded growth. *Nat. Energy* **2016**, *1*, 16010.

[165] Sun, Y. W.; Zhou, J. Q.; Ji, H. Q.; Liu, J.; Qian, T.; Yan, C. L. Single-atom iron as lithiophilic site to minimize lithium nucleation overpotential for stable lithium metal full battery. *ACS Appl. Mater. Interfaces* **2019**, *11*, 32008–32014.

[166] Liu, H.; Chen, X.; Cheng, X. B.; Li, B. Q.; Zhang, R.; Wang, B.; Chen, X.; Zhang, Q. Uniform lithium nucleation guided by atomically dispersed lithiophilic CoN_x sites for safe lithium metal batteries. *Small Methods* **2019**, *3*, 1800354.

[167] Wang, J.; Jia, L. J.; Lin, H. Z.; Zhang, Y. G. Single-atomic catalysts embedded on nanocarbon supports for high energy density lithium-sulfur batteries. *ChemSusChem* **2020**, *13*, 3404–3411.

[168] Gu, J. N.; Zhu, Q.; Shi, Y. Z.; Chen, H.; Zhang, D.; Du, Z. G.; Yang, S. B. Single zinc atoms immobilized on MXene ($Ti_3C_2Cl_x$) layers toward dendrite-free lithium metal anodes. *ACS Nano* **2020**, *14*, 891–898.

[169] Du, Z. G.; Wu, C.; Chen, Y. C.; Cao, Z. J.; Hu, R. M.; Zhang, Y. Z.; Gu, J. N.; Cui, Y. L. S.; Chen, H.; Shi, Y. Z. et al. High-entropy atomic layers of transition-metal carbides (MXenes). *Adv. Mater.* **2021**, *33*, 2101473.